Universidad de Valladolid

ESCUELA DE INGENIERÍAS INDUSTRIALES

UNIVERSIDAD DE VALLADOLID

ESCUELA DE INGENIERIAS INDUSTRIALES

Máster en Ingeniería Industrial

STUDY OF THE GROWTH AND DEVELOPMENT OF A PARTICLE-LADEN RICHTMYER-MESHKOV INSTABILITY USING HIGH ORDER METHODS

Autor:

González Izard, Ricardo

Responsable de Intercambio en la Uva

Parra Santos, Mª Teresa

Universidad de destino

San Diego State University

Valladolid, Septiembre, 2016.

TFM REALIZADO EN PROGRAMA DE INTERCAMBIO

TÍTULO: STUDY OF THE GROWTH AND DEVELOPMENT OF A PARTICLE-LADEN RICHTMYER-MESHKOV INSTABILITY USING HIGH ORDER METHODS

ALUMNO: GONZÁLEZ IZARD, RICARDO

FECHA: SEPTIEMBRE 2016

CENTRO: SAN DIEGO STATE UNIVERSITY

TUTOR: GUSTAAF JACOBS

Resumen

La inestabilidad de Richtmyer-Meshkov (RM) ocurre cuando dos fluidos de distintas densidades son sometidos a una gran aceleración en una dirección opuesta al gradiente de densidades. Para resolver las ecuaciones de Navier-Stokes suponemos un flujo compresible en un dominio cerrado en dos dimensiones. Por un lado, iniciamos el código con una nube de partículas simulando un 4% en volumen y con velocidad inicial nula. Por otro lado, inicializamos la fase gaseosa de acuerdo con una onda de choque con un valor de Mach de 2.8. En el flujo acelerado tras el paso de la onda de choque, parecen dos tipos de inestabilidades de RM: una de ellas es gobernada por los fenómenos de baroclinidad, relacionada con los gradientes de presión y densidad; la otra se encuentra en la fase de partículas, en la cual, al no tener un gradiente de presión, no debería seguir la baroclinidad. En este trabajo mostramos los efectos y similitudes tanto cuantitativas como cualitativas del desarrollo de la fase no baroclínica de la inestabilidad de RM en la fase gaseosa.

Palabras clave: Richtmyer-Meshkov, Inestabilidad, partículas, CFD, baroclinidad.

Abstract

An in-house compressible flow solver is used to study a two-dimensional particle-laden Richtmyer-Meshkov Instability that occurs when two fluids with different densities are subjected to an impulsive acceleration in a direction opposite that of the density gradient. A particle curtain perturbed with a single mode is initialized with a four percent volume density and zero velocity. A carrier gas phase is initialized according to a moving shock wave at Mach 2.8. In the accelerated flow behind the shock, two different RM instabilities occur; one of them is governed by the baroclinic vector which is a measure of how misaligned the gradient of pressure is from the gradient of density. The other is in the particle which in the absence of pressure in the particle phase does not follow in theory of baroclinity. The growth of non-baroclinic RM instabilities is shown to be qualitatively and quantitatively similar to the baroclinic instability because the baroclinic effects in the carrier phase propagate into the particle phase.

Keywords: Richtmyer-Meshkov, Instability, Particles, CFD, baroclinity.

STUDY OF THE GROWTH AND DEVELOPMENT OF A PARTICLE-LADEN RICHTMYER-MESHKOV INSTABILITY FLOW USING HIGH ORDER METHODS

A Thesis

Presented to the

Faculty of

San Diego State University

In Partial Fulfillment

of the Requirements for the Degree

Master of Industrial Engineering

for the University of

Valladolid

---

by

Ricardo González Izard

September 2016

DEDICATION

To my parents,

Nothing worthwhile comes easy. Work, continuous work and hard work, is the only way to accomplish results that last.

– Hamilton Holt

ABSTRACT OF THE THESIS

STUDY OF THE GROWTH AND DEVELOPMENT
OF A PARTICLE-LADEN RICHTMYER-MESHKOV
INSTABILITY FLOW USING HIGH ORDER METHODS

by
Ricardo González Izard
Master of Industrial Engineering for the University of Valladolid
San Diego State University, 2016

An in-house compressible flow solver is used to study a two-dimensional particle-laden Richtmyer-Meshkov Instability that occurs when two fluids with different densities are subjected to an impulsive acceleration in a direction opposite that of the density gradient. A particle curtain perturbed with a single mode is initialized with a four percent volume density and zero velocity. A carrier gas phase is initialized according to a moving shock wave at Mach 2.8. In the accelerated flow behind the shock , two different RM instabilities occur; one of them is governed by the baroclinic vector which is a measure of how misaligned the gradient of pressure is from the gradient of density. The other is in the particle which in the absence of pressure in the particle phase does not follow in theory of baroclinity.The growth of non-baroclinic RM instabilities is shown to be qualitatively and quantitatively similar to the baroclinic instability because the baroclinic effects in the carrier phase propagate into the particle phase.

TABLE OF CONTENTS

LIST OF TABLES

PAGE

LIST OF FIGURES

PAGE

ACKNOWLEDGMENTS

I would like to express my gratitude to Dr. Gustaaf Jacobs from San Diego Sate University, a talented teacher and passionate scientist, who has been a great academic advisor and has guided me through challenging research subjects such as Richtmyer-Meshkov Instability.

I would like to thank Dr. Teresa Parra, from the University of Valladolid, who without, I could not have had the opportunity to do this thesis in this fabulous University.

I cannot describe the gratitude I feel towards my entire family. My parents, Santiago and Marcela, have always taught me the importance of hard work while maintaining and adventurous life. They have given me everything I needed to be successful every day of my life. Without them, none of this would have been possible. My older brother, Santiago, has been a role model for me because of his constant hard work ethic while supporting and advising me. My second older brother, Alejandro's positive outlook in life, even through the hardest of times, has helped me remember what's important. Last but not least, to my youngest brother Jaime who has been excited to hear about my adventures living abroad.

Also to Inés, my partner in this life, my best friend, my love. You have bore my stress and bad moments, giving me the support I need. You have never stopped believing in me. Please, never change.

I can not finish the acknowledgments without mentioning the rest of family, my grandparents, uncles and aunts and cousins. Also to my roommates, lab-mates and of course to my friends, It does not matter if we are in Béjar, Valladolid, London, Madrid, San Diego, or anywhere else in the world; our friendship will never end.

CHAPTER 1
INTRODUCTION

1.1 MOTIVATION

The study of the Shock Waves is an important objective for researchers[16] due to it use in many applications such as jets engines or combustions. The instabilities observed in supernova explosions [14] and inertial confinement fusion (ICF) [9] are being studied but there is more research to do yet. RMI is the result of an accelerated material interface by an incident shock wave and it has also been studied firstly in a planar geometry [1, 2, 5, 9] and recently in curvilinear geometry [11, 12, 33].

Hydrodynamic instabilities at the interface of two materials of different densities are a critical issue in high energy density physics (HEDP). The Rayleigh-Taylor instability (RTI) occurs when a fluid accelerates another fluid of high density [30, 31, 40]. The RTI is ubiquitous in HEDP, such as high Mach number shocks and jets, radiative blast waves and radioactively driven molecular clouds, gamma-ray bursts and accreting black holes, etc. Due to the importance in physics mentioned above, there have been many studies related to RTI from both physical and numerical simulation points of view in the literature.

It was shown [32] that when two inmiscible fluids of different densities are accelerated in a direction perpendicular to their interface, this interface is stable or unstable according to whether the acceleration is directed from the heavier to the lighter fluid or vice versa. The case of gravity, g, pointing downwards is equivalent to the two fluids being accelerated upwards with acceleration, g. The RT unstable configuration is called single-mode or multimode according to the initial interface perturbation being well defined by a sinusoidal wave or being random.

A wide variety of fluid motions can be generated, following the interaction of a shock wave with an interface separating two fluids of different properties. Any perturbation initially present on the interface will, in most cases, be amplified following the refraction of the shock. This class of problems is generally referred to as the Richtmyer - Meshkov instability (RMI). The basic mechanism for the amplification of perturbations at the interface is baroclinic vorticity generation resulting from the misalignment of the pressure gradient of the shock and the local density gradient across the interface. The growth of perturbations soon enters into a nonlinear regime with the appearance of bubbles of light fluid rising into heavy fluid and spikes of heavy fluids falling into light fluids. As the interface between the two fluids becomes

more distorted, secondary instabilities, such as the Kelvin-Helmholtz shearing instability, develop and a region of turbulence and mixing ultimately results.

RM Instability is a special case of RT Instability when the interface is impulsively accelerated by a shock wave, for example. For this reason, it can also be called shock induced RT instability.

The first analytical study on impulsive acceleration of an interface by shock wave was done by Markstein [22] who investigated the interaction of a shock wave with a density interface (flame front). His analytical result was the same as Taylor's [40] result for constant acceleration. But the first real treatment of the impulsive acceleration of the interface by a shock wave was given by Richtmyer [32].He studied the problem of a shock wave impinging on a sinusoidally perturbed interface between two fluids in the linear regime, $i.e., k\omega << 1$. In developing his impulsive model, he assumed that the shock wave is not strong enough to cause perturbation velocities comparable to the speed of sound. Ten years later, Meshkov [28] confirmed, experimentally, Richtmyer's prediction.

The general consensus as to the role that the vorticity generated by the Shocks plays in the perturbation field evolution [41, 45]. The linear theory predictions (essentially series expansions in terms of some adequate functions) agree with numerical simulations, despite the fact that former calculations overestimated the earlier experimental results in shock tubes [27, 45]. Work of L. Holmes *et al* [15] investigates about the growth RMI for negative Atwood numbers and two-dimensional sinusoidal perturbation by comparing experiments, numerical simulations and analytical theories.

1.2 NUMERICAL SCHEME

In this work, the particles are modeled as singular point sources. In high-speed particle-laden flows, the small timescales and range of interphase velocity differences causes the particle phase to rapidly disperse. Although an Eulerian-Eulerian approach is effective at capturing the large scale mixing of the particle and fluid phase [36, 37], dissipation errors arise while tracking the number density in low particle volume fraction environments.

To accurately trace discontinuities while simultaneously resolving small-scale turbulence in the flow, high-order shock-capturing methods have been devised. Essentially Non-Oscillatory (ENO) schemes, first presented by Harten et. al. [13], provide a framework for the implementation of robust high-order finite difference methods for the solution of hyperbolic equations. These schemes maintain a high-order of accuracy while adaptively adjusting the stencil near discontinuities to avoid spurious Gibbs Oscillations. The stencil is adaptively chosen to provide the smoothest reconstruction, thereby avoiding stencils containing discontinuities [19].

Weighted ENO (WENO) schemes, first introduced in [20], improve upon on the adaptive stencil techniques of the ENO scheme. An optimal order of accuracy is obtained at smooth parts of the solution while enough dissipation is retained over discontinuous stencils to damp out oscillations [17]. This is accomplished through a convex combination of all the possible ENO substencils. Improved WENO methods have also been derived, such as the WENO-Z scheme [4, 6, 8, 10], with enhancements to decrease dissipation errors and ensure a high-order accuracy in smoother regions of the flow.

New and more complex WENO schemes are being developing. Recent studies have developed a new fifth order finite difference WENO scheme for solving hyperbolic conservation laws [46], which presents a new WENO scheme as a convex combination of a fourth degree polynomial with linear polynomials in a traditional WENO fashion.

Particles in this scheme take a lot of importance due to the necessity of implement them into the simulations. The motion of the solid phase is governed for laws derived from Navier-Stokes equations. The complexity of the relationship between the particle drag and fluid motion as well as the requirement that numerous coupling parameters be considered, necessitates an accurate, efficient algorithm to represent the behavior of the system. Improving the accuracy of the subgrid model in the macro-scale code requires additional full-resolution experiments, which consume significant computational resources.

1.3 Outline and Contributions

In this thesis the development and growth of the particle-laden Richtmyer-Meshkov Instability is studied comparing the growth rates from simulation and theory. Nowadays we can find many researches in the instability with two fluids with different densities[28, 41, 45] but none of them include a particle-laden flow in Richtmyer-Meshkov Instability. In this work we present results in the non-baroclinic interface with the corresponding governing equations and numerical methods. The particle's cloud is perturbed following a trigonometric function, which reflect a real interface that we can find in many applications mentioned in section 1.1.

Because of the particle phase, we find a resistance in the carrier phase, not only by lowering the velocity but also taking heat from the carrier phase. The trajectory of the particles shows a concentration in the left part of the cloud and also in the middle, due to two vortex located in the upper and bottom sides of the cloud.

RMI growth is governed by baroclinic vector in contrast to particle phase which is non-baroclinic due to the absence of pressure. We find in the growth of this particle phase similarities to the baroclinic interface within a 15% of error. This relation is due to the baroclinic effects in the carrier phase propagate into the particle phase.

The second chapter present Navier-Stokes and all governing equations used to simulate RM Instability. The third chapter explains the theoretical equations of

Raleigh-Taylor Instability leading to RMI growth rate equation. The next chapter explains the numerical methodology as a high-order Eulerian Lagrangian method based on the new Weighted Essentially Non-Oscillatory (WENO) conservative finite difference scheme (WENO-Z) on a uniform mesh. Chapter number 5, explains the problem setup. In the later chapter, we show the discussion and results focusing in the development of the particles produced by Richtmyer-Meshkov Instability. Following last chapter we can find the background (bibliography).

CHAPTER 2

GOVERNING EQUATIONS

2.1 GOVERNING EQUATIONS OF THE CARRIER PHASE

In the particle-source-in-cell (PSIC) method, the Eulerian continuum equations are solved for the carrier flow in the Eulerian frame, while particles are traced along their paths in the Lagrangian frame. In the following, we present the coupled system of Euler equations that govern the gas flow and kinematic equations that govern the particle motion. We shall denote the subscript p for the particle variables and f for the gas variables at the particle position. Variables without subscript refer to the gas variables unless specified otherwise.

2.1.1 Dimensional Form

This section presents the equations of motion for a compressible Newtonian uid, also known as the Navier-Stokes equations. The conservative, dimensional form of the conservation of mass, momentum and energy in Cartesian coordinates are given by

$$\vec{Q}^*_{t^*} + \vec{F}^{a*}_{x^*} + \vec{G}^{a*}_{y^*} + \vec{H}^{a*}_{z^*} = \vec{F}^{v*}_{x^*} + \vec{G}^{v*}_{y^*} + \vec{H}^{v*}_{z^*} + \vec{S}, \tag{2.1}$$

where the superscript * denote dimensional variables, the arrow shows a vector, and

$$\vec{Q}^* = \begin{bmatrix} \rho^* \\ \rho^* u^* \\ \rho^* v^* \\ \rho^* w^* \\ \rho^* e^* \end{bmatrix}, \quad \vec{F}^{a*} = \begin{bmatrix} \rho^* u^* \\ p^* + \rho^* u^{*2} \\ \rho^* u^* v^* \\ \rho^* u^* w^* \\ u^*(\rho^* e^* + p^*) \end{bmatrix}, \quad \vec{G}^{a*} = \begin{bmatrix} \rho^* v^* \\ \rho^* u^* v^* \\ p^* + \rho^* v^{*2} \\ \rho^* v^* w^* \\ v^*(\rho^* e^* + p^*) \end{bmatrix},$$

$$\vec{H}^{a*} = \begin{bmatrix} \rho^* w^* \\ \rho^* u^* w^* \\ \rho^* v^* w^* \\ p^* + \rho^* w^{*2} \\ w^*(\rho^* e^* + p^*) \end{bmatrix}, \tag{2.2}$$

$$\vec{F}^{v*} = \begin{bmatrix} 0 \\ \tau^*_{11} \\ \tau^*_{12} \\ \tau^*_{13} \\ u^*\tau^*_{11} + v^*\tau^*_{12} + w^*\tau^*_{13} + \kappa^* T^*_{x^*} \end{bmatrix},$$

$$\vec{G^{v*}} = \begin{bmatrix} 0 \\ \tau^*_{21} \\ \tau^*_{22} \\ \tau^*_{23} \\ u^*\tau^*_{21} + v\tau^*_{22} + w^*\tau^*_{23} + \kappa^* T^*_{y^*} \end{bmatrix},$$

$$\vec{H}^{v*} = \begin{bmatrix} \tau^*_{31} \\ \tau^*_{32} \\ \tau^*_{33} \\ u^*\tau^*_{31} + v^*\tau^*_{32} + w^*\tau^*_{33} + \kappa^* T^*_{z^*} \end{bmatrix}, \tag{2.3}$$

where,

$$\begin{aligned}
\tau^*_{11} &= 2\mu^*[u^*_{x^*} - (u^*_{x^*} + v^*_{y^*} + w^*_{z^*})/3], \\
\tau^*_{22} &= 2\mu^*[v^*_{y^*} - (u^*_{x^*} + v^*_{y^*} + w^*_{z^*})/3], \\
\tau^*_{33} &= 2\mu^*[w^*_{z^*} - (u^*_{x^*} + v^*_{y^*} + w^*_{z^*})/3], \\
\tau^*_{12} &= \tau^*_{21} = \mu^*[v^*_{x^*} + u^*_{y^*}], \\
\tau^*_{13} &= \tau^*_{31} = \mu^*[w^*_{x^*} + u^*_{z^*}], \\
\tau^*_{23} &= \tau^*_{32} = \mu^*[w^*_{y^*} + v^*_{z^*}].
\end{aligned}$$

The subscript on the stress tensor, τ^*, defines the direction of τ^* and the plane it is acting on, where 1, 2 and 3 denote the x, y and z direction, respectively. In the above equations ρ^* is the density; u^*,v^*, and w^* are the velocities in x^*, y^*, and z^* directions, respectively; p^* is the pressure; T^* is the temperature; the source term,S, accounts for the effect of the particles on the carrier gas and will be discussed in more detail below and $\rho^* e^*$ is the sum of the internal and kinetic energy per unit volume given by

$$\rho^* c^*_v T^* + \frac{1}{2}\rho^*(u^{*2} + v^{*2} + w^{*2}) \tag{2.4}$$

,

where c^*_v is the constant volume specific heat of the fluid; μ^* and κ^* are the fluid dynamic viscosity and conductivity, respectively.

In this work, the following assumptions concerning these equations are made:

- The fluid is Newtonian, i.e. the viscous stresses are postulated to be directly proportional to the rate of deformation of the fluid elements.
- The fluid is continuous, i.e. the smallest length scales occurring in the motion of the fluid flow are very large compared to the mean free path of the molecular motion.
- The fluid has zero bulk viscosity, i.e. $\mu_b^* = 3\lambda^* + 2\mu^* = 0$, where μ_b^* is the bulk viscosity and λ^* is the second coefficient of viscosity. This relation is known as the 'Stokes hypothesis' and reduces the two coefficients in the stress tensor to one. This hypothesis has proven to give adequate results for most gases. For gases that depart far from a local state of chemical equilibrium it might fail [35].
- The heat flux in the energy equation obeys the Fourier's law, *e.g.* $q_{1^*}^* = -\kappa^* T_{x^*}^*$, where q^* is the heat flux and the subscript on q^* indicates its direction.
- The viscosity, conductivity and specific heats of the fluid are assumed to be independent of temperature. In general the viscosity, conductivity, and specific heats vary with temperature, however, for the temperature fluctuations encountered in this work the variations are not very significant ($< 10\%$).
- The fluid is an ideal gas, for which intermolecular forces are negligible, and obeys the equation of state,

$$p^* = \rho^* R^* T^*, \tag{2.5}$$

  where R^* is the gas constant. This equation closes the Navier-Stokes equations, i.e. there are six equations for six unknowns, $\rho^*, u^*, v^*, w^*, p^*$, and T^*.

2.1.2 Non-Dimensional Form

For numerical solution of 2.1 the dimensional form is not favored, since the disparity of the physical variables can generate undesirable errors. Therefore, all variables are non-dimensionalized by reference length L_f^*, density ρ_f^*, velocity U_f^*, and temperature T_f^* scales, leading to the following non-dimensionalization of the variables:

$$\begin{aligned}
\rho &= \rho^*/\rho_f^*, & u &= u^*/U_f^*, \\
v &= v^*/U_f^*, & w &= w^*/U_f^*, \\
T &= T^*/T_f^*, & p &= p^*/(\rho_f^* U_f^{*2}), \\
x &= x^*/L_f^*, & y &= y^*/L_f^*, \\
z &= z^*/L_f^*, & t &= t^* U_f^*/L_f^*.
\end{aligned} \tag{2.6}$$

This leads to the following non-dimenzionalization of 2.1,

$$\vec{Q}_t + \vec{F}_x^a + \vec{G}_y^a + \vec{H}_z^a = \frac{1}{Re_f}(\vec{F}_x^v + \vec{G}_y^v + \vec{H}_z^v) + \vec{S}, \tag{2.7}$$

where

$$\vec{Q} = \begin{bmatrix} \rho \\ \rho u \\ \rho v \\ \rho w \\ \rho e \end{bmatrix}, \quad \vec{F}^a = \begin{bmatrix} \rho u \\ p + \rho u^2 \\ \rho uv \\ \rho uw \\ u(\rho e + p) \end{bmatrix}, \quad \vec{G}^a = \begin{bmatrix} \rho v \\ \rho uv \\ p + \rho v^2 \\ \rho vw \\ v(\rho e + p) \end{bmatrix}, \quad \vec{H}^a = \begin{bmatrix} \rho w \\ \rho uw \\ \rho vw \\ p + \rho w^2 \\ w(\rho e + p) \end{bmatrix}, \tag{2.8}$$

and

$$\vec{F}^v = \begin{bmatrix} 0 \\ \tau_{11} \\ \tau_{12} \\ \tau_{13} \\ u\tau_{11} + v\tau_{12} + w\tau_{13} + \frac{1}{(\gamma-1)M_f^2 Pr} T_x \end{bmatrix},$$

$$\vec{G}^v = \begin{bmatrix} 0 \\ \tau_{21} \\ \tau_{22} \\ \tau_{23} \\ u\tau_{21} + v\tau_{22} + w\tau_{23} + \frac{1}{(\gamma-1)M_f^2 Pr} T_y \end{bmatrix},$$

$$\vec{H}^v = \begin{bmatrix} 0 \\ \tau_{31} \\ \tau_{32} \\ \tau_{33} \\ u\tau_{31} + v\tau_{32} + w\tau_{33} + \frac{1}{(\gamma-1)M_f^2 Pr} T_z \end{bmatrix}, \tag{2.9}$$

where,

$$\begin{aligned} \tau_{11} &= 2[u_x - (u_x + v_y + w_z)/3], \\ \tau_{22} &= 2[v_y - (u_x + v_y + w_z)/3], \\ \tau_{33} &= 2[w_z - (u_x + v_y + w_z)/3], \\ \tau_{12} &= \tau_{21} = v_x + u_y, \\ \tau_{13} &= \tau_{31} = w_x + u_z, \\ \tau_{23} &= \tau_{23} = w_y + v_z, \end{aligned} \tag{2.10}$$

where

$$\rho e = \frac{p}{\gamma - 1} + \rho(u^2 + v^2 + w^2)/2. \tag{2.11}$$

In this equation the inviscid fluxes, denoted with the 'a' superscript, remain unchanged from 2.1. The viscous fluxes, denoted with the 'v' superscript, give rise to the following non-dimensional parameters:

- The reference Reynolds number, which indicates the influence of the viscous fluxes as compared to the advective fluxes, defined as $Re_f = U_f^* L_f^* \rho_f^* / \mu^*$.
- The Prandtl number, which is the ratio of the viscous and thermal diffusivity, defined as $Pr = c_p^* \mu^* / \kappa^*$, where c_p^* is the constant pressure specific heat of the fluid.
- The reference Mach number, $M_f = U_f^* / c^*$, where c^* is the reference speed of sound defined as $c^* = \sqrt{\gamma R^* T_f^*}$, and γ is ratio of the constant pressure specific heat and the constant volume specific heat. In this work M_f is taken equal to unity, so that the reference velocity is equal to the reference speed of sound.

The ideal gas equation of state in non-dimensional form is given by

$$p = \frac{\rho T}{\gamma M_f^2}. \tag{2.12}$$

2.2 Governing Equations of the Dispersed Phase

Dispersed phase flows are flows in which one phase, the dispersed phase, is not materially connected. These include gas-particle and liquid-particle flows in which the particles constitute the dispersed phase. The phase is solved by tracking each particle individually with the analytical solution of the flow around a spherical particle.

2.2.1 Dimensional Form

The droplet/particle phase, also called the dispersed phase, is solved by tracking each particle individually with the analytical solution of the flow around a spherical particle. Technically, this does not allow for the term DNS to be used for the simulation of two-phase flow where the full Navier-Stokes equations would have to be solved around every particle. This is computationally not feasible. The term DNS is, however, generally accepted for this type of two-phase flow simulation.

The kinematic equations describing the particle position $\vec{x}_d^*$ and velocity $\vec{v}_d^*$, are given as

$$\frac{d\vec{x}_d^*}{dt^*} = \vec{v}_d^*, \tag{2.13}$$

$$m_d^* \frac{d\vec{v}_d^*}{dt^*} = \sum F^*(t^*). \tag{2.14}$$

2.14 constitutes Newton's second law, where m_d^* is the particle mass, and $F^*(t^*)$ denotes the forces acting on the particle. The derivation of an analytical expression for $F^*(t^*)$ in 2.14 has been subject of many studies [25, 29, 34]. No closed form has yet been obtained. However, in

most practical cases for which the density of the particle is much greater than the density of the carrier phase, and the particle size is much smaller than the smallest length scale of the carrier phase, it suffices to consider just the quasi-steady viscous drag force on the particle. Stokes derived the equation for this force [44], which is given by

$$F^*_{Stokes} = C_{Ds} 6\pi \rho^*_{fd} \nu^* a^*_d (\vec{v}^*_{fd} - \vec{v}^*_d). \tag{2.15}$$

Here, ν^* is the kinematic viscosity of the fluid, defined as μ^*/ρ^*, the subscript 'fd' depicts a carrier phase variable at the particle position, and the subscript d represents a particle variable. C_{Ds} is a correction factor for high Reynolds numbers, given by [21]

$$C_{Ds} = 1 + \frac{Re_d^{2/3}}{6} \qquad Re_d < 1000, \tag{2.16}$$

where $Re_d = \rho^*_{fd} d^*_d |\vec{v}^*_{fd} - \vec{v}^*_d|$ is the particle Reynolds number. a^*_d and d^*_d are the particle radius and diameter, respectively. Substituting $m^*_d = 4\pi a^{*3}_d \rho^*_d/3$ and 2.15 into 2.14 leads to the following equation for the droplet velocity;

$$\frac{d\vec{v}^*_d}{dt^*} = C_{Ds} \frac{18\nu^* \rho^*_{fd}}{\rho^*_d d^{*2}_d} (\vec{v}^*_{fd} - \vec{v}^*_d), \tag{2.17}$$

This equation is valid under the following assumptions:

- The particle is spherical.
- The flow around the particle is that of an incompressible, continuous fluid. Quantitatively this means that the Knudsen number, Kn <0.3, where Kn is defined as the ratio of the free molecular path, ℓ, over a characteristic length scale, which in case of the particle is its diameter, d^*_d.
- Viscous forces dominate over convective forces, i.e. the particle Reynolds number is smaller than one. The correction factor, C_{Ds} allows for the use of 2.17 up to Re_d=1000.
- The dispersed phase is dilute, i.e. particle-particle interaction through for example collision or wake interaction, is negligible. This will be satisfied if the average particle separation is larger then five times the particle diameter [21].
- Body forces such as gravitational or electromagnetical forces are not present.
- Particle rotation is negligible, i.e. $|\omega^*_d 2a^*_p/|\vec{v}^*_{fd} - \vec{v}^*_d|$, where ω^*_d is the rotation of the particle, is smaller than one.
- Unsteady forces, or forces due to gradients in the fluid are negligible.

In certain flows and for certain particle parameters, the last assumption might not be valid. Examples are highly accelerating flows or flows with large velocity gradients and for particles with small density compared to the fluid [21]. Unsteady forces, Saffman, and Faxen forces might then contribute significantly to the force on the particle. In this work, a flow

where other forces than the Stokes drag become important, is considered and the Basset-Boussineq-Oseen (BBO) equation is employed to track the particles. Aside from the Stokes drag, the BBO equation takes into account the Basset history force, virtual or added mass effects and forces that result from acceleration of the fluid element in the vicinity of the particle, also called the stress gradient effect. The Faxen forces are not taken into account.

The Basset history force result from the temporal development of the particle wake and becomes important when there are strong fluid accelerations at time scales on the order of convection over the particle surface. Different forms are found in literature [29, 25, 26]. In this work, the following form described in [29] is employed:

$$F^*_{Basset}(t) = C_H \rho^*_{fd} a^{*2}_d \sqrt{\pi \nu^*} \int_{t_0}^{t} \frac{d(\vec{v}^*_{fd} - v^*_d)}{d\tau} \frac{d\tau}{\sqrt{(t^* - \tau)}}, \tag{2.18}$$

where C_H is an empirical correction factor for high Reynolds numbers, and is expressed as

$$C_H = 2.88 + \frac{3.12}{(1 + A_c)^3}. \tag{2.19}$$

Here,

$$\frac{d}{dt^*} = \frac{\partial}{\partial t^*} + v^*_{d-x^*} \frac{\partial}{\partial x^*} + v^*_{d-y^*} \frac{\partial}{\partial y^*} + v^*_{d-z^*} \frac{\partial}{\partial z^*}, \tag{2.20}$$

and A_c is the relative acceleration factor, given by

$$A_c = \frac{|\vec{v}^*_{fd} - \vec{v}^*_d|^2 / d^*_d}{|d(\vec{v}^*_{fd} - \vec{v}^*_d)/dt^*|} \tag{2.21}$$

The virtual mass effect depicts the added force that a particle experiences due to inertial effects of the fluid surrounding the particle. Effectively, the particle becomes "heavier" due to this effect, hence the term virtual or added mass. The expression used for this force in this work was derived in [29], and is

$$F^*_{virtual}(t^*) = C_A \frac{4}{3} \pi a^{*3}_d \rho^*_{fd} \frac{d(\vec{v}^*_{fd} - \vec{v}^*_d)}{dt^*}, \tag{2.22}$$

where C_H is an empirical correction factor for high Reynolds numbers, and is expressed as,

$$C_A = 1.05 - \frac{0.066}{{A_c}^2 + 0.12}. \tag{2.23}$$

The stress gradient effect results from the acceleration of the local fluid element or the stress on the particle owing to the undisturbed flow. The expression derived by [25] is used for this force and is

$$F^*_{stress-gradient}(t^*) = \frac{4}{3} \pi a^{*3}_d \rho^*_{fd} \frac{D\vec{v}^*_{fd}}{Dt^*} \tag{2.24}$$

where D/Dt^* is given by,

$$\frac{D}{Dt^*} = \frac{\partial}{\partial t^*} + v^*_{fd-x^*}\frac{\partial}{\partial x^*} + v^*_{fd-y^*}\frac{\partial}{\partial y^*} + v^*_{fd-z^*}\frac{\partial}{\partial z^*} \tag{2.25}$$

In sheared flows, the velocity gradient induces a quasi-steady lift that will have significant influence on the particle force. In [34] the one-dimensional form of this quasi-steady lift force was derived. The three-dimensional form is derived through rotation of the one-dimensional form and is given in [21] as,

$$F^*_{Saffman} = \frac{1.61\rho^*_{fd}d^{*2}_d}{\sqrt{|\Omega^*_{fd}|}}(\vec{v^*}_{fd} - \vec{v^*}_d) \times \vec{\Omega}^*_{fd}, \tag{2.26}$$

where Ω^* is the vorticity vector of the fluid at the particle position.

Substituting 2.15, 2.18, 2.22, 2.24 and 2.26 into 2.14 leads to the BBO equation for the particle velocity,

$$\begin{aligned}\frac{d\vec{v^*}_d}{dt^*} = \frac{18\nu^*\rho^*_{fd}}{\rho^*_d d^{*2}_d}(\vec{v^*}_{fd} - \vec{v^*}_d) + \frac{3}{4}\frac{C_H\sqrt{\nu^*}\rho^*_{fd}}{\sqrt{\pi}\rho^*_d a^*_d}\int_{t^*_0}^{t^*}\frac{d(\vec{v^*}_{fd} - \vec{v^*}_d)/d\tau}{\sqrt{t^* - \tau}}d\tau \\ +C_A\frac{\rho^*_{fd}}{\rho^*_d}\frac{d}{dt^*}(\vec{v^*}_{fd} - \vec{v^*}_d) + \frac{\rho^*_{fd}}{\rho^*_d}\frac{D(\vec{v^*}_{fd})}{Dt} + \frac{3.07\rho^*_{fd}}{\sqrt{\rho^*_d d^*_d|\Omega^*_{fd}|}}(\vec{v^*}_{fd} - \vec{v^*}_d) \times \vec{\Omega^*}_{fd},\end{aligned} \tag{2.27}$$

From the first law of thermodynamics [24] and Fourier's law for heat transfer, the following equation for the particle temperature, T^*_d, may be derived,

$$m^*_d c^*_p\frac{dT^*_d}{dt^*} = 2Nu\pi a^*_d\kappa^*(T^*_{fd} - T^*_d). \tag{2.28}$$

In this equation Nu is the Nusselt number corrected for Re_d >1, and is expressed as [23],

$$Nu = 2 + 0.6Re^{0.5}_d Pr^{0.33} \tag{2.29}$$

Substituting for the particle mass leads the following equation for the particle temperature,

$$\frac{dT^*_d}{dt^*} = 6Nu\frac{\kappa^*}{c^*_p}\frac{1}{\rho^*_d d^*_d 2}(T^*_{fd} - T^*_d). \tag{2.30}$$

In the derivation of this equation, all assumptions made in the derivation of the Stokes drag must be satisfied. In addition the following assumption must hold:

- The temperature distribution in the particle is uniform. This is valid for Biot numbers, Bi <0.1, which is defined as $Bi = h^* d^*_d/\kappa^*$, where h^* is the convective heat transfer coefficient.

2.2.2 Non-Dimensional Form

2.27 is non-dimensionalized with the same reference variables used in Section 2.1.2 leading to the non-dimensionalized form of the BBO equation:

$$\frac{d\vec{v}_d}{dt} = \frac{C_{Ds}}{St}(\vec{v}_{fd} - \vec{v}_d) + \frac{0.2C_H}{(\varepsilon St)^{1/2}}\int_{t_0}^{t}\frac{d(\vec{v}_{fd} - \vec{v}_d)/d\tau}{\sqrt{t-\tau}}d\tau$$
$$+C_A\frac{1}{\varepsilon}\frac{d}{dt}(\vec{v}_{fd} - \vec{v}_d) + \frac{1}{\varepsilon}\frac{D(\vec{v}_{fd})}{Dt} + \frac{0.727}{(\varepsilon St|\vec{\Omega}|)^{1/2}}(\vec{v}_{fd} - \vec{v}_d)\times\vec{\Omega}_{fd}, \tag{2.31}$$

where ε is the ratio of the particle to fluid densities

$$\varepsilon = \frac{\rho_d^*}{\rho_{fd}^*} = \frac{\rho_d}{\rho_{fd}}. \tag{2.32}$$

St is the Stokes number defined as

$$St = \frac{t_d}{t_f} = \frac{\rho_d^* d_d^{*2} U_f^*}{18\mu^* L_f^*} = \frac{\rho_d d_d^2 Re_f}{18}, \tag{2.33}$$

where $t_d = \rho_d^* d_d^{*2}/18\mu^*$ represents the particle response time and $t_f = L_f^*/U_f^*$ is a characteristic flow time. The temperature in non-dimensional form is,

$$\frac{dT_d}{dt} = \frac{Nu}{3PrSt}(T_{fd} - T_d). \tag{2.34}$$

2.3 SOURCE TERM S

Each particle generates a momentum and energy that affects the carrier flow. The volume averaged summation of all these contributions gives a continuum source contribution on the momentum and energy equation in 2.7 as:

$$S_m(x) = \sum_{i=1}^{N_p} K(x_p, x)W_m \tag{2.35}$$

$$S_e(x) = \sum_{i=1}^{N_p} K(x_p, x)(W_m V_p + W_e) \tag{2.36}$$

where $K(x,y) = K(|x-y|)/V$is a normalized distribution function that distributes the influence of each particle onto the carrier flow. This distribution function should ideally be a dirac delta function but is most often a regularized delta function [39]. W_m and W_e are weigh functions describing the momentum and energy contribution of one particle, respectively. These equations are given by

$$W_m = m_p f_1 \frac{(T - T_p)}{\tau_p} \tag{2.37}$$

and

$$W_e = m_p \frac{Nu}{3Pr\tau_p}(T - T_p) \tag{2.38}$$

The term m_p is the mass of one spherical particle which can be derived from τ_p. N_p is the total number of particles in a finite volume V. The factor f_1 is given by

$$f_1 = \frac{3C_{dss}}{4 \cdot 18} \tag{2.39}$$

CHAPTER 3

THEORY RICHTMYER-MESHKOV EQUATION

To explain the basis of Richtmyer-Meshkov Instability we study the basis of the Rayleigh-Taylor Instability first. RM instability is a special case of RT instability when the interface is impulsively accelerated by a shock wave, for example. For this reason, it can also be called shock induced RT instability.

We consider a flow in the x-direction, which in the lower half-space z $<$ 0 has velocity U_1 and density $\rho 1$, whereas in the upper half-space the gas streams with U_2 and has density $\rho 2$. In addition, there can be a homogeneous gravitational field g pointing into the negative z-direction.

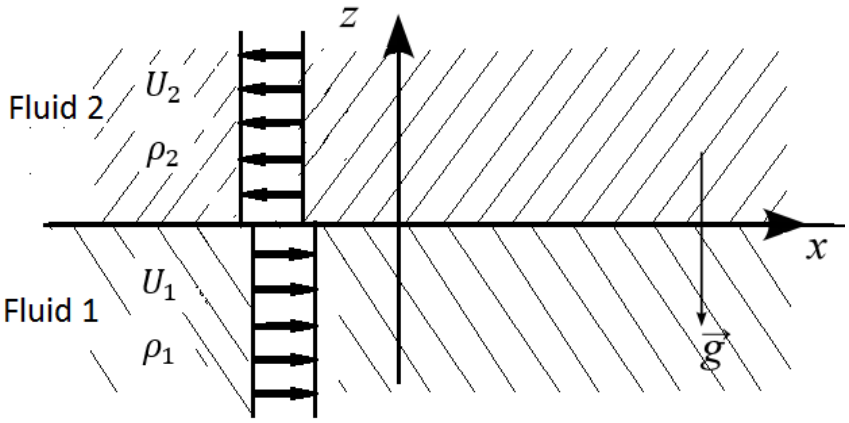

Figure 3.1. Initial scheme of RTI. Two different fluids moving at velocities U_1 and U_2 under the effect of the gravity.

Let us assume the flow can, at least approximately, be treated as an incompressible potential flow. Let the velocity field in the upper and lower halves be given by

$$\mathrm{upperhalf} : \mathrm{v}_2 = \nabla\phi_2 \tag{3.1}$$

$$\mathrm{lowerhalf} : \mathrm{v}_1 = \nabla\phi_1 \tag{3.2}$$

The equation of motion for an incompressible gas with constant density can be written as

$$\frac{\partial \mathbf{v}}{\partial t} + (\mathbf{v} \cdot \nabla)\mathbf{v} = g - \nabla(\frac{P}{\rho}) \tag{3.3}$$

If we use the identity

$$(\mathbf{v} \cdot \nabla)\mathbf{v} = \nabla(\frac{1}{2}v^2) - \nabla \times \mathbf{v} \tag{3.4}$$

Together with the assumption of a potential flow $\mathbf{v} = \nabla\Phi$ and hence $\nabla \times \mathbf{v} = 0$, we can write the equation of motion as

$$\nabla\frac{\partial \phi}{\partial t} + \nabla(\frac{1}{2}v^2) - g + \nabla(\frac{P}{\rho}) = 0 \tag{3.5}$$

Writing the gravitational acceleration as $g = -ge_z$ this implies

$$\frac{\partial \Phi}{\partial t} + (\frac{1}{2}v^2) + ge_z + \frac{P}{\rho} = constant \tag{3.6}$$

which is Bernoullis theorem. We now assume for the velocity potentials in the upper and lower half

$$\Phi_2 = U_2 x + \phi_2 \tag{3.7}$$

$$\Phi_1 = U_1 x + \phi_1 \tag{3.8}$$

where ϕ_1 and ϕ_2 are infinitesimal perturbations.

Let us further introduce a function that describes the z-location of the interface

$$\xi(x, t) = z \tag{3.9}$$

The total time derivative of this equation hence describes the velocity of the interface in the z-direction. This must match the fluid velocities in the z direction of the two phases, yielding for example for the 1-side:

$$\frac{\partial \xi}{\partial x}\frac{\partial \Phi_1}{\partial x} + \frac{\partial \xi}{\partial t} = \frac{\partial \Phi_1}{\partial z} \tag{3.10}$$

This gives first

$$\frac{\partial \xi}{\partial t} + \frac{\partial \xi}{\partial x}(U_1 + \frac{\partial \phi_1}{\partial x}) = \frac{\partial \phi_1}{\partial z} \tag{3.11}$$

$$\frac{\partial \xi}{\partial t} + \frac{\partial \xi}{\partial x}(U_2 + \frac{\partial \phi_2}{\partial x}) = \frac{\partial \phi_2}{\partial z} \tag{3.12}$$

Hence we obtain the two equations:

$$\frac{\partial \xi}{\partial x}U_1 + \frac{\partial \xi}{\partial t} = \frac{\partial \phi_1}{\partial z} \tag{3.13}$$

$$\frac{\partial \xi}{\partial x} U_2 + \frac{\partial \xi}{\partial t} = \frac{\partial \phi_2}{\partial z} \tag{3.14}$$

We can now relate the perturbed interface to the unperturbed state via the Bernoulli equation. For example, for phase 1, we can write

$$\frac{\partial \phi_1}{\partial t} + \frac{1}{2}(U_1 + \frac{\partial \phi_1}{\partial x})^2 + g\xi + \frac{P_1}{\rho_2} = \frac{1}{2}U_1^2 + \frac{P_0}{\rho_1} \tag{3.15}$$

where the left hand side is the perturbed state, the right hand side is the unperturbed state, with the initial pressure P_0. An analogous equation can also be written down for phase 2, with an equal initial pressure P_0. In addition, the pressures P1 and P2 must be equal. Equating the two pressures from the two Bernoulli equations and keeping only leading order terms leads to

$$\rho(\frac{\partial \phi_1}{\partial t} + U_1 \frac{\partial \phi_1}{\partial x} + g\xi) = \rho(\frac{\partial \phi_2}{\partial t} + U_2 \frac{\partial \phi_2}{\partial x}) + g\xi) \tag{3.16}$$

To this end we make an eigen mode analysis.

$$\phi_1 = \phi_1(z) e^{i(kx - \omega t)} \tag{3.17}$$

which respects the symmetry of the problem. Because ϕ_1 fulfills the Laplace equation, we get

$$\frac{\partial^2 \phi_1}{\partial z^2} = k^2 \phi_1 \tag{3.18}$$

which solutions are

$$\phi_1(z) \propto e^{kz} \tag{3.19}$$

$$\phi_1(z) \propto e^{-kz} \tag{3.20}$$

However, the latter solution can be discarded because of boundary conditions, since for $z \to \infty$ we need to have an unperturbed state with $\phi_1 \to 0$. In a similar way, we same solutions for ϕ_2 and conclude that its z-dependence can only go as $\phi_2(z) \propto e^{-kz)}$. This therefore leads to the following three equations for a single Fourier mode:

$$\phi_1 = \hat{\phi_1} e^{kz} e^{i(kx - wt)} \tag{3.21}$$

$$\phi_2 = \hat{\phi_2} e^{-kz} e^{i(kx - wt)} \tag{3.22}$$

$$\xi = \hat{\xi} e^{i(kx - wt)} \tag{3.23}$$

Here ϕ_1, ϕ_2, and ξ are the corresponding mode amplitudes. Inserting these mode equations into the differential equations 3.13, 3.14 and 3.16 yields three algebraic equations:

$$-iw\hat{\xi} + U_1 ik\hat{\xi} = k\hat{\phi}_1 \tag{3.24}$$

$$-iw\hat{\xi} + U_2 ik\hat{\xi} = k\hat{\phi}_2 \tag{3.25}$$

$$\rho_1(-iw\hat{\phi}_1 + U_1 ik\hat{\phi}_1 + g\hat{\xi}) = \rho_2(-iw\hat{\phi}_2 + U_2 ik\hat{\phi}_2 + g\hat{\xi}) \tag{3.26}$$

Last equation is called generalized eigenvalue problem with which it is possible to develop other equations governing different instabilities, such as Raleigh-Taylor, Richtmyer-Meshkov or Kelvin Hermhotz Instabilities. Non-trivial solutions with $\hat{\xi} \neq 0$ are possible for:

$$\omega^2(\rho_1 + \rho_2) - 2\omega k(\rho_1 U_1 + \rho_2 U_2) + k^2(\rho_1 U_1^2 + \rho_2 U_2^2) + (\rho_2 - \rho_1)kg = 0, \tag{3.27}$$

which is the *dispersion relation*. Unstable, exponentially growing mode solutions appear if there are solutions for ω with negative imaginary part.

If we consider that the fluid is at rest, $U_1 = U_2 = 0$. This dispersion relation simplifies to

$$\omega^2(\rho_1 + \rho_2) + (\rho_2 - \rho_1)kg = 0, \tag{3.28}$$

And making clear ω:

$$\omega^2 = \frac{(\rho_1 - \rho_2)kg}{(\rho_1 + \rho_2)} = Akg \tag{3.29}$$

Here g is directed from ρ_2 to ρ_1 ($\rho_2 > \rho_1$) . If A < 0, ω grows exponentially with time. This means the interface becomes unstable. This is the so-called Rayleigh-Taylor instability. It is in essence buoyancy driven and leads to the rise of lighter material in a stratified atmosphere. The free energy that is tapped here is the potential energy in the gravitational field.

Also notice that for an ideal gas, arbitrary small wavelengths are unstable, and those modes will also grow fastest. If A > 0, the interface oscillates, showing stability.

$$\int_{\partial\Omega} \omega = \int_{\Omega} d\omega.$$

which produces

$$\int_{\partial\Omega} \omega = \int_{\Omega} d\omega.$$

Richtmyer used the result of Taylor (Equation 3.29) replacing the constant acceleration g by an impulsive one, $g = [u]\delta_D(t)$, where $[u]$ is the change in the velocity of the interface imparted by the shock wave and $\delta_D(t)$ is the Dirac Delta function. Substituting this value of g in Equation 3.29 and derivating one time, the following expression for the growth rate is obtained:

$$\frac{d\omega}{dt} = k[u]A\omega_0 \tag{3.30}$$

where ω_0 is the initial amplitude.

From equation 3.30 we easily can see that the amplitude w grows with the time as opposed to the exponential growth in the RT case.Also, both light-heavy ($A > 0$) and heavy-light ($A < 0$) cases are unstable in contrast to the RT case which has only one situation being unstable. For $A > 0$, the initial amplitude continues growing from the start, while for $A < 0$, the amplitude first becomes zero, reverses sign and then grows according to Equation 3.30.

Richtmyer also did linearized compressible computations using finite difference techniques and found that if the initial compression of the interface and of the fluids is taken into account ($i.e.$, using post-shock values $A^{'}$and $\omega^{'}$in equation 3.30). The corrected impulsive model thus proposed by Richtmyer was

$$\frac{d\omega}{dt} = k[u]A^{'}\omega_0^{'} \tag{3.31}$$

where the primed quantities are post-shock values.This model neglects viscosity, surface tension, and other stabilizing mechanisms.

If we set the gravitational field to zero in equation 3.27, g = 0, we have the situation of a pure shear ow. Each flow has a different velocity $|U_1 - U_2|$. In this case, the solutions of the dispersion relation are given by

$$\omega = \frac{k(\rho_1 U_1 + \rho_2 U_2)}{\rho_1 + \rho_2} \pm i\frac{\sqrt{\rho_1\rho_2}}{\rho_1 + \rho_2}|U_1 - U_2| \tag{3.32}$$

If the velocities are different, in an ideal gas there is an imaginary growing component. This means that a small wave-like perturbation at an interface will grow rapidly into large waves that take the form of characteristic Kelvin-Helmholtz billows. In the non-linear regime reached during the subsequent evolution of this instability the waves are rolled up, leading to the creation of vortex like structures. As the instability grows fastest for small scales (high k), with time the billows tend to get larger and larger.

As the Kelvin-Helmholtz instability basically means that any sharp velocity gradient in a shear flow is unstable in a freely streaming fluid, this instability is particularly important

for the creating of fluid turbulence. Under certain conditions, some modes can however be stabilized against the instability. This happens for example if we consider shearing with $U_1 \neq U_2$ in a gravitational field $g > 0$. Then the dispersion relation has the solutions.

$$\omega = \frac{k(\rho_1 U_1 + \rho_2 U_2)}{\rho_1 + \rho_2} \pm i \frac{\sqrt{-k^2 \rho_1 \rho_2 (U_1 - U_2)^2 - (\rho_1 + \rho_2)(\rho_1 - \rho_2) k g}}{\rho_1 + \rho_2} |U_1 - U_2| \quad (3.33)$$

It will become stable if two conditions are met:

1. $\rho_1 > \rho_2$ which means that the lighter fluid needs to be on top (otherwise we would have in any case a Rayleigh-Taylor instability).
2. $(U_1 - U_2)^2 < \frac{(\rho_1+\rho_2)(\rho_1-\rho_2)g}{k\rho_1\rho_2}$

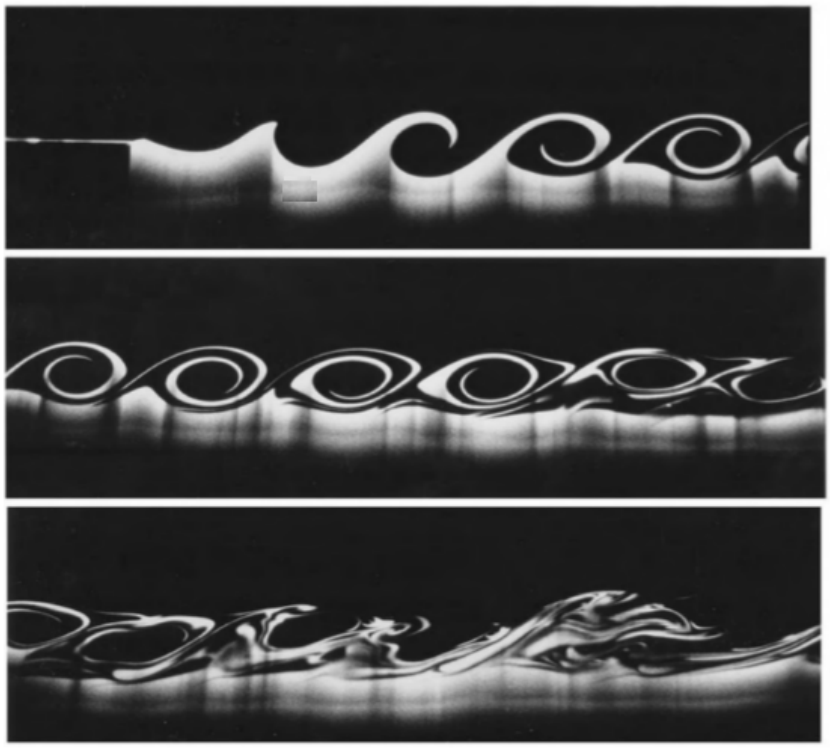

Figure 3.2. Development of a KelvinHelmholtz instability in the laboratory. The upper and faster moving layer is slightly less dense than the lower layer. At first, waves form and overturn in a two-dimensional fashion but, eventually, three-dimensional motions appear that lead to turbulence and complete the mixing.

CHAPTER 4

NUMERICAL METHODOLOGY

The numerical method used in this work is the high-order Eulerian Lagrangian method based on the Weighted Essentially Non-Oscilatory (WENO) conservative finite difference scheme (WENO-Z) on a uniform mesh. This method is described in more details in the following sections.

4.1 CARRIER PHASE SOLVER

In the numerical simulation of compressible flows modeled by means of hyperbolic conservation laws in the form

$$\frac{\partial \mathbf{u}}{\partial t} + \nabla \mathbf{F(u)} = 0 \tag{4.1}$$

Without loss of generality, we will restrict our discussion to the one dimensional scalar case. Extensions to the system of equations and higher spatial dimensions present no extra complexity.

Consider a uniformly spaced grid defined by the points $x_i = i \triangle x, i = 0, ..., N$, which are also called cell centers, with cell boundaries given by $x_{i+\frac{\nabla x}{2}} = x_i + \frac{\triangle x}{2}$ where x is the uniform grid spacing in x-direction. The semi-discretized form of last equation yields a system of ordinary differential equations:

$$\frac{du_i(t)}{dt} = - \left. \frac{\partial f}{\partial x} \right|_{x=x_i} \qquad i = 0, \cdots, N. \tag{4.2}$$

Where $u_i(t)$ is a numerical approximation to the point value $u_i(x_i, t)$. A conservative difference formulation for hyperbolic conservation laws requires high-order consistent numerical fluxes at the cell boundaries in order to form the flux differences across the uniformly spaced cells. The conservative property of the spatial discretization is obtained by implicitly defining the numerical flux function $h(x)$ as

$$f(x) = \frac{1}{\Delta x} \int_{x-\frac{\Delta x}{2}}^{x+\frac{\Delta x}{x}} h(\xi) d\xi \tag{4.3}$$

Such that spatial derivate is exactly approximated by a conservative finite difference formula at the cell boundaries,

$$f(x) = \frac{1}{\Delta x} \int_{x-\frac{\Delta x}{2}}^{x+\frac{\Delta x}{2}} (h_{i+\frac{1}{2}} - h_{i-\frac{1}{2}}) \tag{4.4}$$

where $h_{i\pm\frac{1}{2}} = h(c_{i\pm\frac{1}{2}})$

At the cell faces, $h_{i\pm\frac{1}{2}}$ are interpolated from the known flux function $F(x)$ at the cell centers, $f_i = F(x_i)$. The classical fifth order WENO scheme uses a 5-points global stencil S^5, which is subdivided into three substencil S_0, S_1, S_2 with each substencil containing three grid cells as shown in Figure 4.1.

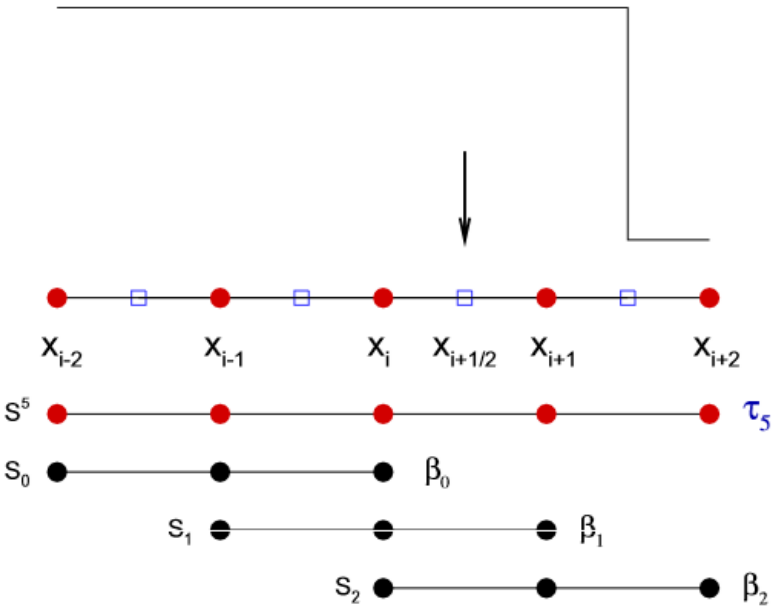

Figure 4.1. The computational uniform grid x_i and the 5-points stencil S^5, composed of three 3-points stencils S_0, S_1, S_2, used for the fth-order WENO reconstruction step.

The fifth order polynomial approximation $\hat{f}_{i+\frac{1}{2}} = h_{i\pm\frac{1}{2}} + \bigcirc(\Delta x^5)$ is built through the convex combination of the interpolated values $\hat{f}^k(x \pm \frac{1}{2})$, in which $\hat{f}^k(x)$is the third degree polynomial below, defined in each one of the stencilsS_k:

$$\hat{f}_{i\pm\frac{1}{2}} = \sum_{k=0}^{2} w_k \hat{f}^k(x_{i\pm\frac{1}{2}}) \tag{4.5}$$

where

$$\hat{f}^k(x \pm \frac{1}{2}) = \hat{f}^k_{i\pm\frac{1}{2}} = \sum_{j=0}^{2} c_{kj} f_{i-k+j}, i = 0, ..., N. \tag{4.6}$$

The $c_{kj}$are Lagrangian interpolations coefficients, which depends on the left-shift parameter $k = 0, 1, 2$, but not on the values f_i.

The weights w_k are defined as

$$w_k = \frac{\alpha_k}{\sum_{i=0}^{2} \alpha_i}, k = 0, 1, 2. \tag{4.7}$$

The coefficients $d_1 = \frac{3}{10}, d_2 = \frac{3}{5}, d_3 = \frac{1}{10}$are called the ideal weights since they generate the central upstream fifth-order scheme for the 5-points stencil S^5. We refer to α_z^kas the unnormalized weights.

The regularity (smoothness) of $\hat{f}^k(x)$ in the substencil S^k is measured by the lower order local smoothness indicators

$$\beta_k = \sum_{l=1}^{2} \Delta x^{2l-1} \int_{x_{i-\frac{1}{2}}}^{x_{i+\frac{1}{2}}} \left(\frac{d^l}{dx^l} \hat{f}^k(x) \right)^2 dx. \tag{4.8}$$

The expression of the β_k in terms of the cell averaged values of $f(x), f_i$ are given by

$$\beta_0 = \frac{13}{12}(f_{i-2} - 2f_{i-1} + f_i)^2 + \frac{1}{4}(f_{i-2} - 4f_{i-1} + 3f_i)^2, \tag{4.9}$$

$$\beta_1 = \frac{13}{12}(f_{i-1} - 2f_i + f_{i+1})^2 + \frac{1}{4}(f_{i-1} - f_{i+1})^2, \tag{4.10}$$

$$\beta_2 = \frac{13}{12}(f_i - 2f_{i+1} + f_{i+2})^2 + \frac{1}{4}(3f_i - 4f_{i+1} + f_{i+2})^2. \tag{4.11}$$

The idea of the weights definition is that on smooth parts of the solution, the smoothness indicators β_k are all small and about the same size, generating weights w_k that are good approximations to the ideal weighs.

To satisfy the sufficient conditions for fifth-order convergence, we use a new smoothness indicator of the higher order than the classical smoothness indicatorβ_k. We denote it byτ_5 and it is simply defined as the absolute difference between β_0 and β_2 at x_i,namely,

$$\tau_5 = |\beta_0 - \beta_2|. \tag{4.12}$$

The most important properties of τ_5 are:

- If S^5 does not contain discontinuities, then $\tau_5 = \bigcirc(\Delta x^5) << \beta_k$ for $k = 0, 1, 2$
- If the solution is continuous at some of the S_k, but discontinuous in the whole S^5, then $\beta_k << \tau_5$, for those k where the solution is continuous
- $\tau_5 \leq max\beta_k$

The new smoothness indicator β_z^k is defined as

$$\beta_k^z = \left(\frac{\beta_k + \epsilon}{\beta_k + \tau_5 + \epsilon} \right), k = 0, 1, 2, \tag{4.13}$$

and the WENO-Z weight is defined as

$$\omega_k^z = \frac{\alpha_k^z}{\sum_{i=0}^{2} \alpha_i^z}, k = 0, 1, 2. \tag{4.14}$$

with

$$\alpha_k^z = \frac{d_k}{\beta_k^z} = d_k \left(1 + \frac{\tau_5}{\beta_k + \epsilon} \right) \tag{4.15}$$

where ϵ is a small number (in this work we use $\epsilon = 10^{-12}$) used to avoid the division by zero. All β_k^z are smaller than unity and they are all close to 1 at the smooth parts of the solution. They are in fact the normalization of the classical smoothness indicator β_k by the higher order information contained in τ_5.

4.2 PARTICLE-MESH METHOD

To solve the particle phase we use a Lagrangian tracing of individual computational particle paths. Lagrangian tracking of the particles consists of three stages per particle, including searching the element a particle is located in, interpolating the eld variables to the particle location, and pushing the particle forward with a time integration method matching the WENO integration scheme.

If we locate the Eulerian cell in which the particle resides, $\mathbf{i}_p$ is computed on the structured grid,

$$\mathbf{i_p} = INT \left[\frac{\mathbf{x_p} - \mathbf{x_0}}{\mathbf{x_N} - \mathbf{x_0}} \right] (\mathbf{i_N} - \mathbf{i_0}) + \mathbf{i_0} \tag{4.16}$$

where $\mathbf{x_p}$ are the particle locations, $\mathbf{x_0}$ and $\mathbf{x_N}$ are the lower and upper bounds of the domain respectively and $\mathbf{i_0}$ and $\mathbf{i_N}$ are the first and last cell node indices. the INT function truncates the bracketed quotient to an integer, causing the searching algorithm to the choose the lower host cell node and thereby creating an erroneous numerical bias in the solution. For most cases, the grid cells are small enough that this numerical error is negligible. However, for symmetric problems, the host cells below the centerline are adjusted by adding one to $\mathbf{i_p}$.

In smooth flow areas without shocks, the WENO-Z method uses a central difference scheme. Under these conditions, centered interpolation to the particle position is more accurate and therefore preferred. Lagrange interpolating polynomials of degree k,

$$\mathbf{P}_k(x_p) = \sum_{i=i_p-k/2}^{i_p+k/2} \mathbf{Q}(x_i l_i(x_p) \tag{4.17}$$

where ip represents the nearest node to the particle position found in Equation 4.16 are used to compliment the WENO scheme. The number of points k should be equal to the number of points used as the order of the WENO scheme [67]. In the case of the fifth order WENO scheme the Lagrange interpolating polynomials would be of degree $k = 5$.

ENO interpolation is only necessary in WENO-domains identified by the smoothness indicator. In those domains, the interpolating points are determined based on the smoothness of the function indicated by the divided differences. The k-th degreed divided differences are determined first. The 0-th order divided differences of Q are defined by:

$$\mathbf{Q}[x_i] = \mathbf{Q}(x_i) \tag{4.18}$$

The j-th degree divided difference for $j \geq 1$ are defined by

$$\mathbf{Q}[x_i, \cdots, x_{i+j}] = \frac{\mathbf{Q}[x_{i+1}, \cdots, x_{i+j}] - \mathbf{Q}[x_i, \cdots, x_{i+j+1}]}{x_{i+j-x_i}} \tag{4.19}$$

Starting from a two point stencil, x_{ip}, x_{ip+1}, the interpolation stencil is expanded to k points based on a comparison of the divided differences of the the increasing order at i_p. The smallest second order divided differences at i_p of the two potential three points stencils $min\mathbf{Q}[x_{ip-1}, x_{ip}, x_{ip+1}], \mathbf{Q}[x_{ip}, x_{ip+1}, x_{ip+2}]$ indicates the smoothest interpolation stencil and is therefore chosen. This procedure is repeated until a k point interpolant is found.

The Lagrange interpolant in equation 4.17 then interpolates to the particle position.

In Fig. 4.2, we give an example of a typical ENO stencil close to a shock. We find the nearest grid point to the left of the particle. The magnitude of the first order divided differences at this grid point are larger than the divided differences to the left because of the shock jump. The stencil is therefore extended to the left. The same holds for the divided difference of a higher-order than one. So, the ENO stencil will be preferential one-sided to the left of the particle if the particle is located on the cell including a shock.

In two dimensions, the same procedure can be used along the separate dimension on the tensor grid. The divided differences are determined along horizontal and vertical lines in the grid.

An example of two dimensional ENO stencil is shown in Fig. 4.3. The particle's nearest grid point is found to the left and the bottom of the particle. The left and the bottom point of the ENO stencil are determined by comparison of the divided difference along the horizontal and vertical line crossing the nearest grid point. If a particle is located in a cell with a shock, then the ENO is one-sided to the left and bottom of the particle. We note that if two

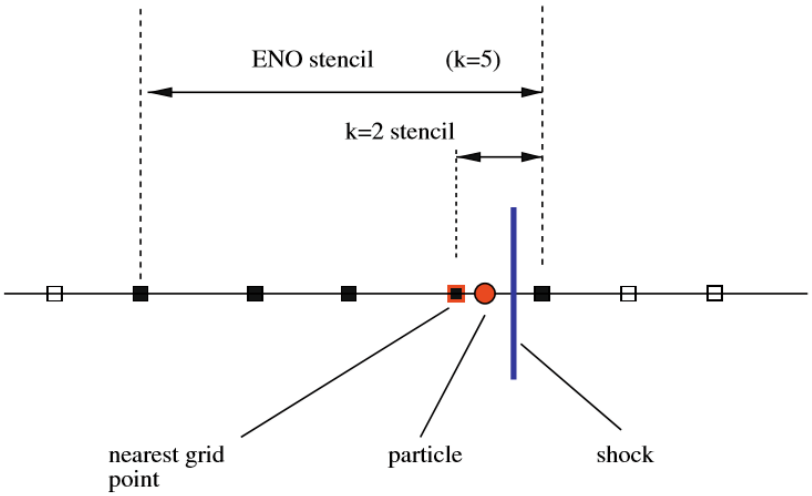

Figure 4.2. One dimensional ENO stencil for interpolation to a particle located near a shock. The interpolation stencil is determined based on the divided differences at the particle's nearest grid point to the left of the particle.

shocks cross the k interpolation stencil, then this procedure will fail to recognize the second shock. We did not encounter stability problems.

To finish this section, we also give an example of a three-dimensional ENO stencil in Fig. 4.4. The particle's nearest grid points is found to the back, bottom, and left of the particle. The back, bottom and left points of the ENO stencil are determined by comparison of the divided difference along the x, y, an z grid lines crossing the nearest grid point. If a particle is located in a cell with a shock, then the ENO is one-sided to the back, bottom and left of the particle.

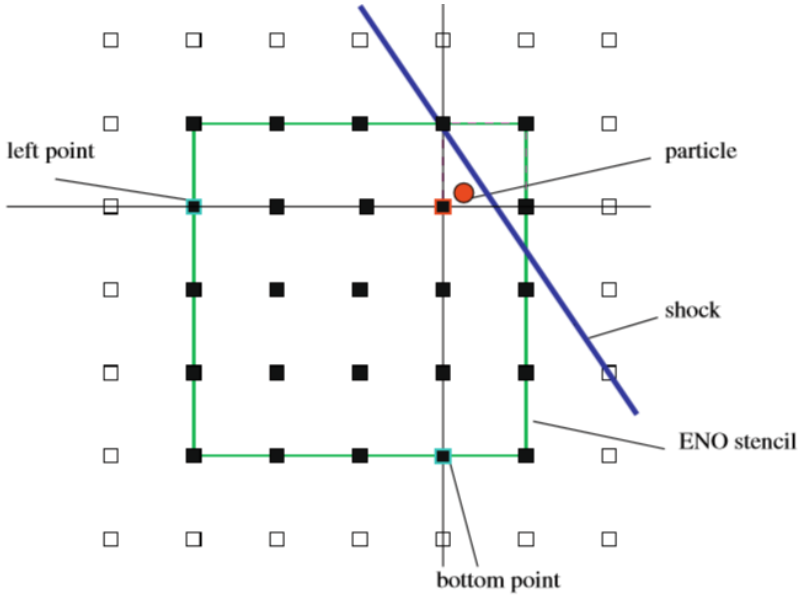

Figure 4.3. Two-dimensional ENO stencil for interpolation to a particle located near a shock. The left and the bottom point of the interpolation stencil is determined based on the divided differences along the horizontal grid lines and the vertical grid lines at the particle's nearest grid point to the left and the bottom of the particle position.

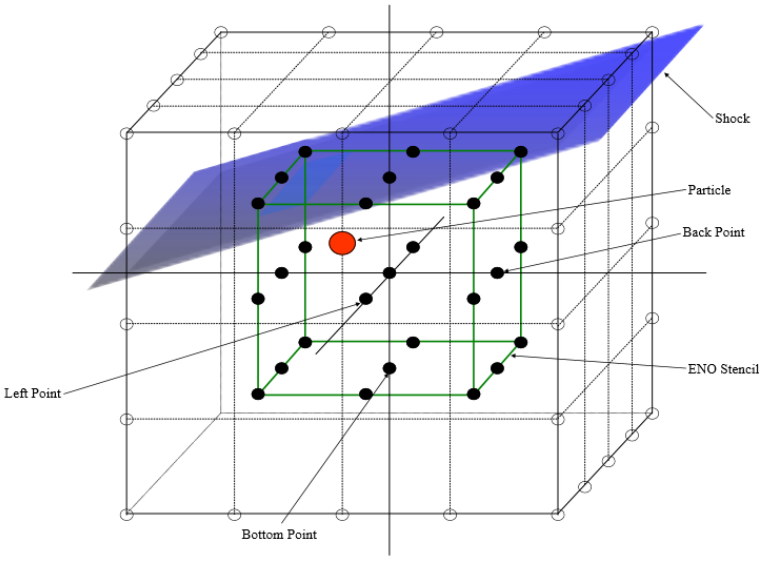

Figure 4.4. Three-dimensional ENO stencil for interpolation to a particle located near to a shock. The back, left and bottom points of the interpolation stencil were determined based on the divided differences along the x, y and z grid lines at the particle's nearest grid point.

CHAPTER 5

PROBLEM SETUP

In this experiment, we simulate a 4% volume fraction cloud of 135,000 computational particles 5.1. The particle response time and density are, $\tau_p = 1.7845 \times 10^3$ and $\rho_p = 1200$, respectively. We have three different elements that we need to take into account: The particle's cloud, fluid 1 (Shock Wave) and fluid 2. A schematic figure is provided to show the basis of the experiment (Fig. 5.1).

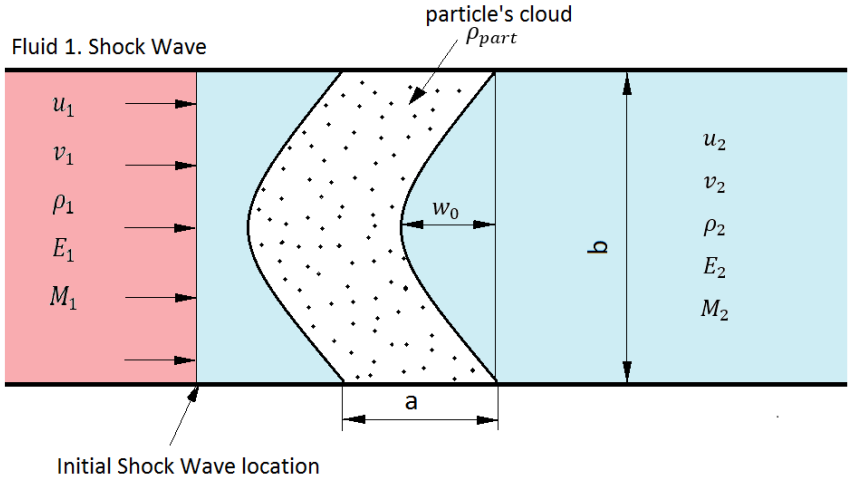

Figure 5.1. Schematic figure showing the initial setup of the simulation, which involves two different kind of fluids and a particle's cloud. Fluid 1 is considered the Shock Wave and Fluid 2 and the particles are initialized with zero velocity. The particle's cloud is located in Fluid 2.

The particles are initially evently distributed with zero velocity in a perturbed cloud streching a width of 0.2941 (in x-direction) and a height of 0.2 (in y-direction) with 150×900 particles. The function of the initial perturbation follows a cosine profile allocating the particles uniformly. The x and y location of each particle is governed by the next equations.

$$\mathbf{x_p} = x_0 + \mathbf{k} \cdot \delta x_p + w_0 \cdot cos(\frac{2\pi}{T_{cloud}} \cdot b \cdot \mathbf{y_{loc}}) \tag{5.1}$$

$$\mathbf{y_p} = -\frac{b}{2} + \mathbf{j} \cdot \delta y_p \tag{5.2}$$

where $\mathbf{x_p}$ and $\mathbf{y_p}$ are the position of the particle in x and y direction respectively, x_0 is the initial location of the cloud, dx_{part} is the distance between particles in x-direction and is defined as $\delta x_p = \frac{a}{n_{partx}}$ where a is the width of the cloud and n_{partx} is the number of particles in x-direction,δy_{part} is the distance between particles in y-direction and is defined as $\delta y_{part} = \frac{b}{n_{party}}$ where b is the height of the cloud and n_{party} is the number of particles in y-direction. The variable $\mathbf{k}$ is a counter for each row of particles starting at 1 up to $npartx$ adding 1 when we change to another particle while **j** is a counter for each column of particles starting at 1 up to $nparty$ adding 1 when we have allocated a complete row of particles. w_0 is the initial amplitude of the cloud, T_{cloud} is the period of the cosine function which for equation 5.1 is 1 and $\mathbf{y_{loc}}$ is the position in y direction of the current particle's row and is defined as $\mathbf{y_{loc}} = \frac{j-1}{n_{party}}$.

We consider a WENO mesh with 800 x 200 points in the x and y directions respectively. This domain has been chosen as t The computational domain spans an area of -0.5 to 6.5 in the x-direction where we can see all the instabilities produced by RMI. The height is from -0.1 to 0.1 in the y- direction. A uniform inflow boundary condition is specified at $x = -0.15$ and periodic boundary conditions are specified in upper and bottom sizes of the domain. To close the boundaries, the right size of the domain has outflow boundary conditions. We use a Reynolds Number around the particles of $Re_f = 9.6503 \cdot 10^5$ to compute the drag force according to Davis et. al.[7]. Experiment is performed with an initial uniform flow where the fluid Mach number is $M_1 = 2.8$.

For a summary of the initial parameters of the particle phase see Table 5.1. The CFL number is 0.5.

The initial setup establishes a Shock Wave with u_1, v_1, ρ_1, E_1 and M_1, moving through a fluid 2, with u_2, v_2, ρ_2, E_2 and M_2, where u is the velocity in x direction, v is the velocity in y direction, ρ is the density of the fluid, E is the sum of the inertial and kinetic energy and M is the Mach number. In the fluid 2 there is located a particle's cloud initialized with zero velocity describing a perturbation following the function explained in equations 5.1 and 5.2. At some point, it hits the particle's cloud initializing the Richtmyer-Meshkov Instability.

Table 5.1. Summary of the initial particle parameters to reproduce Richtmyer-Meshkov Instability with a particle's cloud with a volume fraction of 4%.

Name	Symbol	Value
Particle Response Time	τ_p	$1.7845 \cdot 10^3$
Density of the particles	ρ_p	1200
Reynolds Number	Re_f	$9.6503 \cdot 10^5$
Cloud Width	a	0.298
Cloud Height	b	0.2
Volume fraction	V	0.04
Initial Cloud amplitude	w_0	0.1
Period	T_{cloud}	1.0
Start location of the cloud	x_0	0.0
Distance between particles in x-direction	δx_{part}	$1.96066 \cdot 10^{-3}$
Distance between particles in y-direction	δy_{part}	$2.222 \cdot 10^{-4}$
CFL	CFL	0.5

Table 5.2. Fluid parameters for both fluid 1 (Shock Wave) and Fluid 2, including the initial velocity in x and y directions, density, energy and Mach number.

Name	Symbol	Value
Velocity in x direction	u_1	8.824
Velocity in y direction	v_1	0
Density	ρ_1	3.66
Sum of inertial and kinetic energy	E_1	33.0775
Initial Mach number	M_1	2.8
Velocity in x direction	u_2	0
Velocity in y direction	v_2	0
Density	ρ_2	1
Sum of inertial and kinetic energy	E_2	2.5
Initial Mach number	M_2	0

CHAPTER 6

NON-BAROCLINIC DRIVEN FLOW INTERFACE

In this subsection we will study the development of the particle cloud along the domain. Once the Shock Wave starts moving from left to right, it hits the cloud. Therefore, the particles located more to the left are the first on being affected by the shock, so they are the first particles that are going to move. Because of that, we are going to find a small compression in the width of the cloud followed by a linear growth [32].

The Shock Wave is moving to the right as we set in the initial conditions. Just after the cloud, the density profile is lower due to the lower pressure. To counteract the lower Pressure and density, the Temperature increases considerably following ideal gas equation, as shown in Fig. 6.1. A secondary mushroom is created in the fluid, which we will refer here and beyond as a baroclinic driven flow interface.

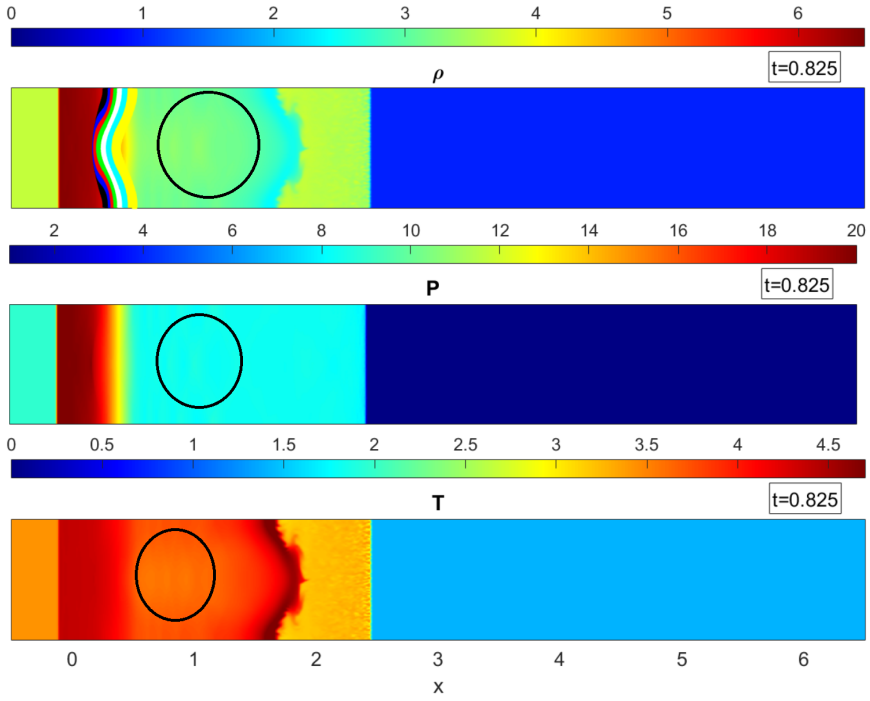

Figure 6.1. Density profile with the particles, Pressure of the fluid and the Temperature of the fluid at time=0.825. After the particles cloud, we encounter a lower density and pressure, but a higher Temperature due to the heat transfer from the carrier phase to the particle phase.

The vorticity is the local angular rate of rotation, so is the tendency for elements of the fluid to spin. To calculate this parameter in two dimensions we use the next equation,

$$\Omega = \frac{\partial v}{\partial x} - \frac{\partial u}{\partial y} \tag{6.1}$$

where Ω is the vorticity, u is the velocity in x direction and v is the velocity in y direction.

The particles are concentrated at the beginning of the mushroom (at the left) due to the first impact of the Shock Wave. At this point we display a number density called Φ which shows the concentration of the particles in the cells; this variable is discussed in appendix A.1. In Fig.6.2 we show at time=2.2 how this particles get concentrated.

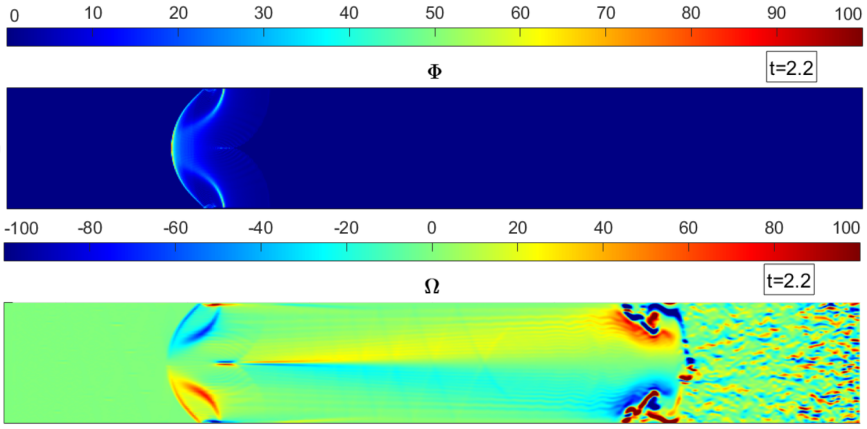

Figure 6.2. Variable Φ showing the concentration of the particles at time=2.2. The particles get concentrated at the left of the cloud and also we find two high density inside the cloud. The vorticity profile shows two clearly vortex in the cloud leading the transportation of the particles to the upper and bottom sizes respectively.

Once the Shock wave has hit the particles cloud we can see in Fig. 6.3 the particles in the left of the cloud get compressed. If we have a look at $\tilde{U}$, the velocity in x direction is higher in the upper and bottom right sizes of the cloud. Also, in the middle of the cloud the particles are slower. Thus, if in the middle the particles are slow and in both ends they are fast, the cloud amplitude is going to grow in time.

If we let run the simulation some more time as shown in Fig.6.4 we easily can see that the amplitude of the cloud is growing with time. The secondary mushroom also starts growing, as shown in section 6.1.

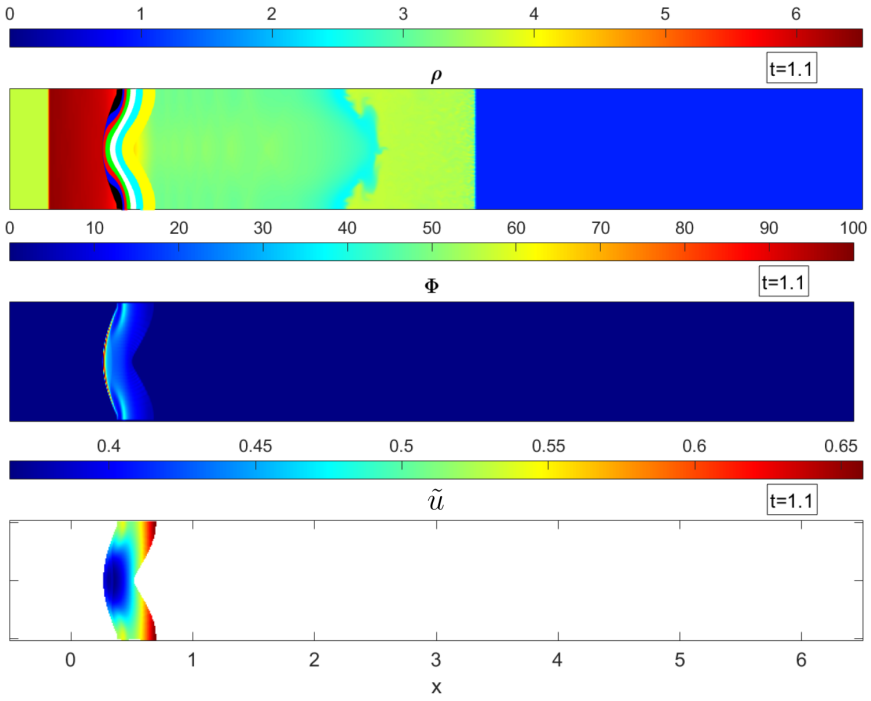

Figure 6.3. Particles in a density profile, number density ϕ and average velocity $\tilde{U}$ profiles in Time=1.1. The particles start concentrating as explained in the section as well as the higher velocity of the particles in the upper and bottom part of the cloud.

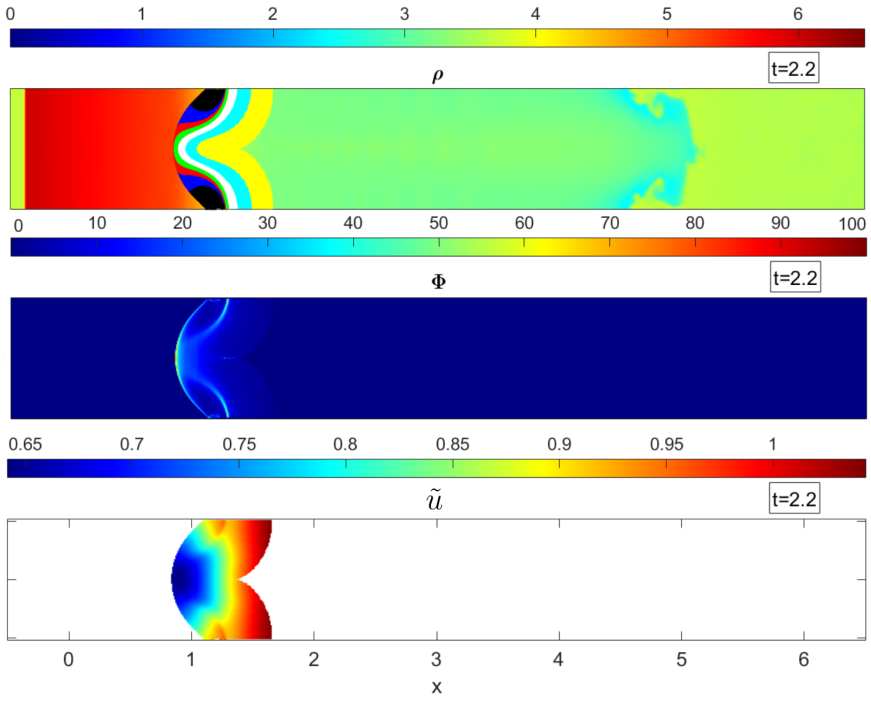

Figure 6.4. Particles in a density, ϕ and $\tilde{U}$ profiles in Time=2.2. The transmitted Shock is taking the form of a mushroom and the particles are gain velocity.

In Fig.6.5 we show this vorticity profile. In the cloud we can see in red a positive value of the vorticity which means that $\frac{\partial v}{\partial x}$ is higher than $\frac{\partial u}{\partial y}$ and the cloud try to rotate in a counter-clockwise direction as viewed from above. In the other hand, blue color means a rotation in a clockwise direction. Because of these, this particles are tending to join together in $y = 0$ leading to a reduction of the velocity in the already mentioned center line.

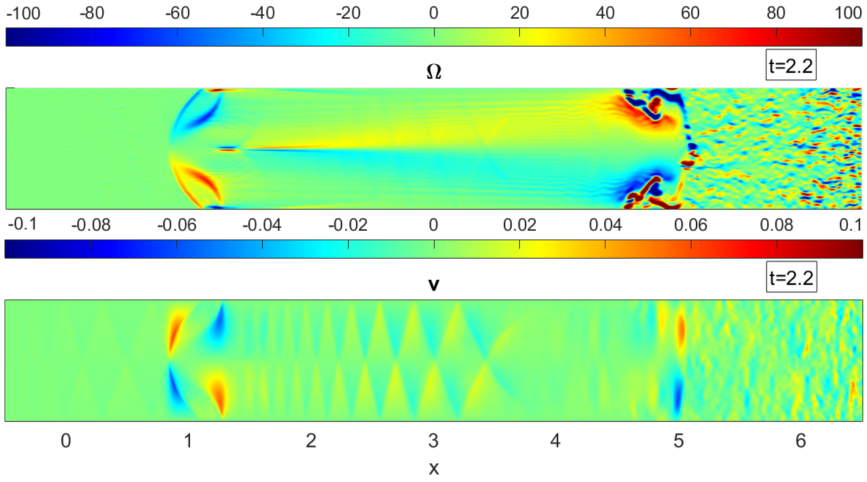

Figure 6.5. Vorticity profile involved in the particle cloud at time = 2.2. It is generating clockwise vorticity on the upper side of the perturbation and counterclockwise vorticity on the bottom.

In Fig.6.5 we also can confirm the rotation of the particle's cloud. Red color in v (velocity in y-direction) means that the particles are going up the domain while blue color means that the particles are going down the domain (in y-direction). If we look at the left size of the figure, for the upper half of y red colors move particles to the upper part, and then blue color move again the particles to the middle of the cloud.

In the next display we show the simulation in later times where we can easily see Richtmyer-Meshkov Instability (time=3.3) in Fig. 6.6

In this point of the simulation another two particle clouds are hitting our cloud in the upper and bottom part of y domain coinciding with the periodic boundary conditions in $y = -0.1$ and $y = 0.1$. This phenomenon pushes the particles up and down in $y = -0.1$ and $y = 0.1$ respectively, helping in the compression of the particle's cloud. In Fig. 6.7 we mark in red the area where the effect of the boundary conditions are perfectly visible.

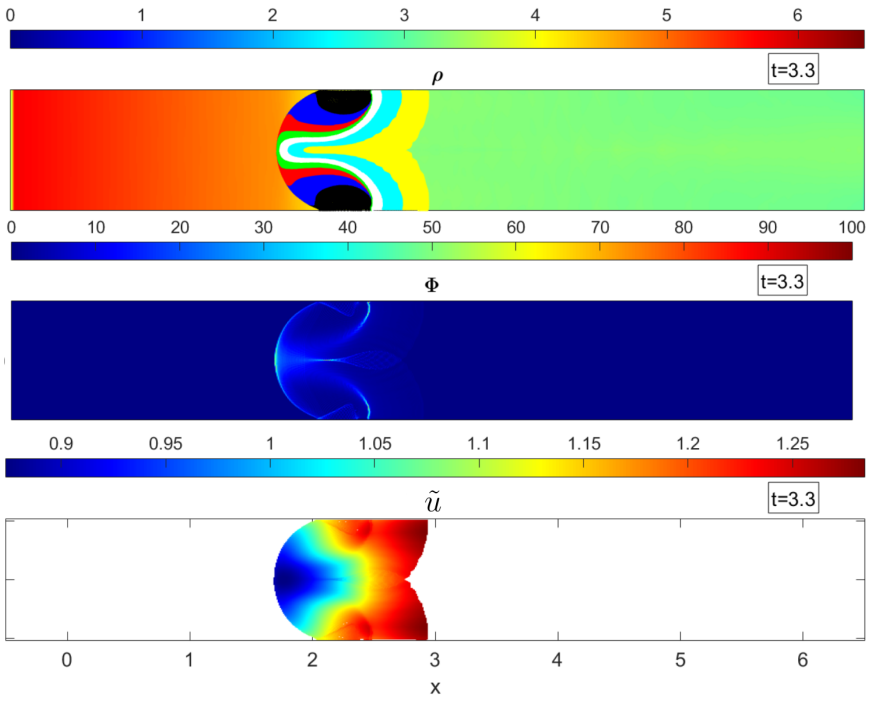

Figure 6.6. Particles in a density profile, ϕ and $\tilde{U}$ profiles in Time=3.3. Black particles, which were the first in being hit are now concentrated at the left side of the cloud as well as in the upper and bottom side. This is due to the higher initial velocity in combination in vorticity generated in the cloud.

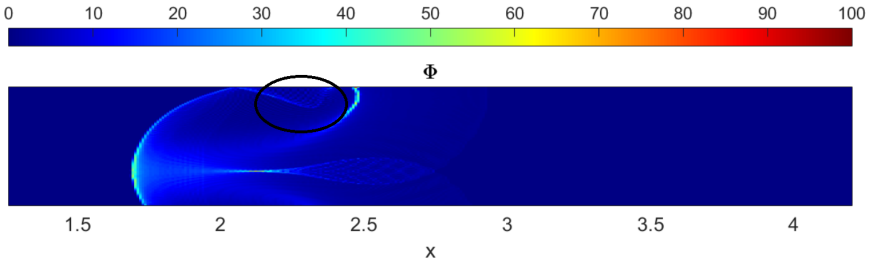

Figure 6.7. ϕ showing periodic boundary conditions established in $y = 0.1$ and $y = -0.1$.

It is known that when we have more particles in one area, this particles are going to be slower [7]. If we have a look to the Mach number in Fig. 6.8 we can see that in the middle of the cloud the velocity is lower than in other areas of the cloud. The more particles we have, more resistance they are going to put forward. We find in the upper and bottom sizes of the cloud a higher Mach number, this is due to the effect of the concentration of the particles in the middle of the cloud. This particles all together act as a solid and it put difficulties to the fluid, so the fluid round this concentrated particles leading the dispersion through the upper and bottom parts of the cloud, and given the particles higher velocities.

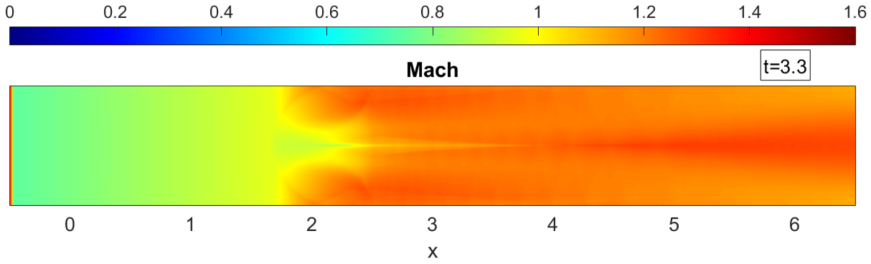

Figure 6.8. Mach number in time=3.3. Yellow color means a subsonic flow so at the middle of the cloud, the flow is subsonic allowing the instability growth in the upper and bottom side.

We also can appreciate a big area colored in yellow in Fig. 6.8 where $M < 1$, which means than the flow is not supersonic. Because of this, we are going to find a reflected shock moving to the left as shown in Fig.6.9 up tp -0.5 in x direction. In Appendix B we provide the complete simulation of this parameter.

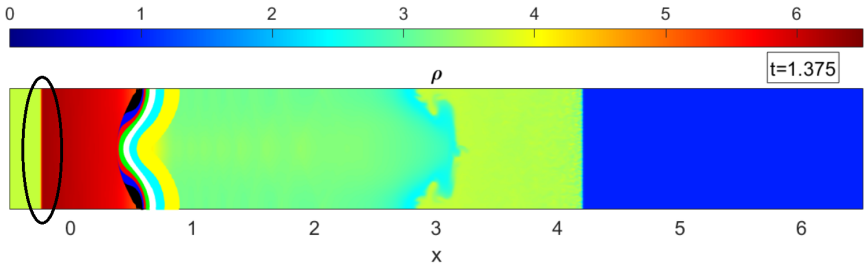

Figure 6.9. Reflected Shock at the left size of the particle's cloud due to the subsonic flow. This Reflected Shock will move until *x≈-0.5*

At later times, the particle's cloud continues growing (Fig. 6.10) linearly in time according with Equation. 6.2. In the middle cloud, the yellow particles hits to each other side forming a cone as shown in Fig. 6.10.

$$\frac{d\omega}{dt} = k[u]A^{'}\omega_0^{'} \tag{6.2}$$

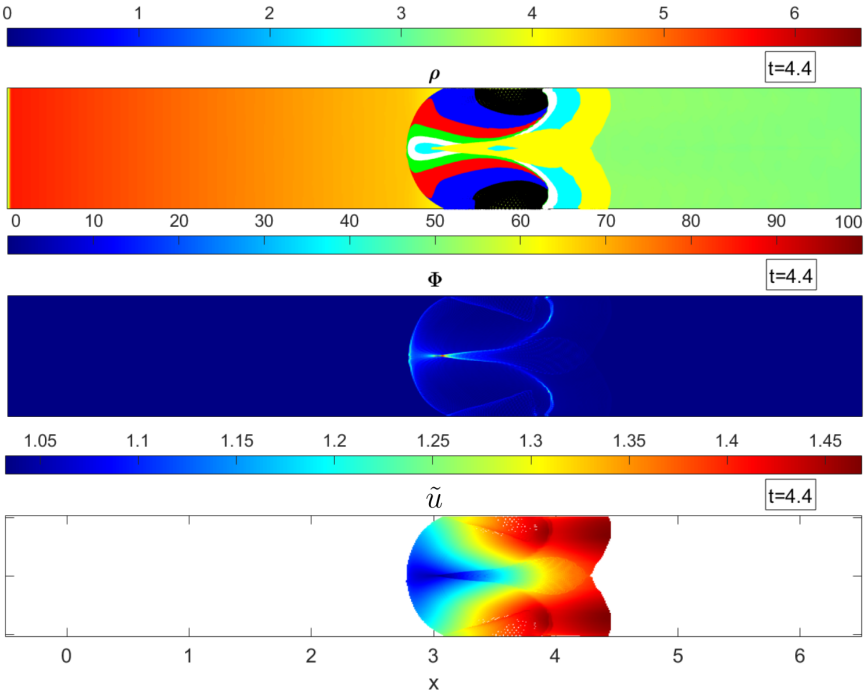

Figure 6.10. Figures shown the particles in a density, ϕ and $\tilde{U}$ profiles in Time=4.4

d

6.1 Growth Of Richtmyer-Meshkov Instability

Equation 6.3 shows the growth rate Richtmyer-Meshkov Instability. As we have described before, this growth is theoretically linear in contrast to Rayleigh-Taylor Instability which growth rate function is exponential.

$$\frac{d\omega}{dt} = k[u]A^{'}\omega_0^{'} \tag{6.3}$$

where the primed quantities are post-shock values. In the equation w is the amplitude of the Instability; k is the wave number, explained as $k = \frac{2\pi}{\lambda}$ where $\lambda = 0.2$;the initial amplitude is $w_0^{'} = 0.1$; $A^{'}$ is the Atwood number post-shock, so ones the Shock wave hits the cloud we will find a mix between the particles and the fluid. Because of that, we introduce a new density of the mix, which is called ρ_{mix} and is defined as

$$\rho_{mix} = \rho_{part}V + \rho_1(1 - V) \tag{6.4}$$

where the volume concentration of the particles is $V = 0.04$ (4%) and ρ_1 is the density of the Shock Wave.

Thus, the Atwood number we have to take into account is

$$A^{'} = \frac{\rho_{mix} - \rho_1}{\rho_1 + \rho_{mix}} \tag{6.5}$$

The variable $[u]$ as we explained in is the change in the velocity of the interface imparted by the shock wave so we defined as $\frac{d\tilde{u}_{part}}{dt}$ in the first step of the simulation at $time = 0.06875$, where $\tilde{u}_{part}$ is the average velocity of the particles in early times.

We use three different values of ρ_{part}. In the first simulation we use a value of $\rho_{part} = 1200$, the second one $\rho_{part} = 2400$ and the last one $\rho_{part} = 8800$. When we change the density of the particle, the diameter is function of the density and it is defined as

$$d_{part} = \sqrt{\frac{18\tau_p}{Re_f \rho_{part}}} \tag{6.6}$$

where d_{part} is the diameter of the particle. Because of this, τ_p is particle response time and Re_f is the Reynolds Number around the particle. If ρ_{part} is higher, d_{part} is going to be smaller changing the Volume Fraction of the cloud.

In the next Tables 6.1, 6.2 and 6.3, we summary the parameters used to calculate RM growth. When we use a higher density of the particles, the diameter

Table 6.1. Parameters involved for the calculation of RM instability growth rate when $\rho_{part} = 1200$. The volume fraction in this case is 4%.

Name	Symbol	Value
Volume Fraction	V	0.04
Density of the Shock Wave	ρ_1	3.66
Density of the particles	ρ_{part}	1200
Density of the mix	ρ_{mix}	51.5136
Atwood number	$A^{'}$	0.86733
Wave number	k	31.41592
Initial amplitude of the cloud	$w_0^{'}$	0.1
Change in the velocity of the interface	$[u]$	0.1658
RM growth rate 1	$\frac{dw_1}{dt}$	0.4527

Table 6.2. Parameters used for the calculation of RM instability growth rate when the $\rho_{part} = 2400$. The volume fraction in this case is 2.82%

Name	Symbol	Value
Volume Fraction	V	0.0282
Density of the Shock Wave	ρ_1	3.66
Density of the particles	ρ_{part}	2200
Density of the mix	ρ_{mix}	65.71
Atwood number	$A^{'}$	0.8961
Wave number	k	31.41592
Initial amplitude of the cloud	$w_0^{'}$	0.1
Change in the velocity of the interface	$[u]$	0.1338
RM growth rate 2	$\frac{dw_2}{dt}$	0.3766

Table 6.3. Parameters used for the calculation of RM instability growth rate when the $\rho_{part} = 8800$. The volume fraction in this case is 1.47%

Name	Symbol	Value
Volume Fraction	V	0.0147
Density of the Shock Wave	ρ_1	3.66
Density of the particles	ρ_{part}	8800
Density of the mix	ρ_{mix}	133.52
Atwood number	$A^{'}$	0.9464
Wave number	k	31.41592
Initial amplitude of the cloud	$w_0^{'}$	0.1
Change in the velocity of the interface	$[u]$	0.08
RM growth rate 3	$\frac{dw_3}{dt}$	0.2381

From last three tables we obtain the growth rate of RM Instability, which following Equation 3.30 is linear in time. The higher the number density is, the lower is the growth rate. In Fig. 6.11 we provide results of the different simulations including the theoretical growth rate. In all simulations we find an initial compression of the cloud followed by a linear growth.

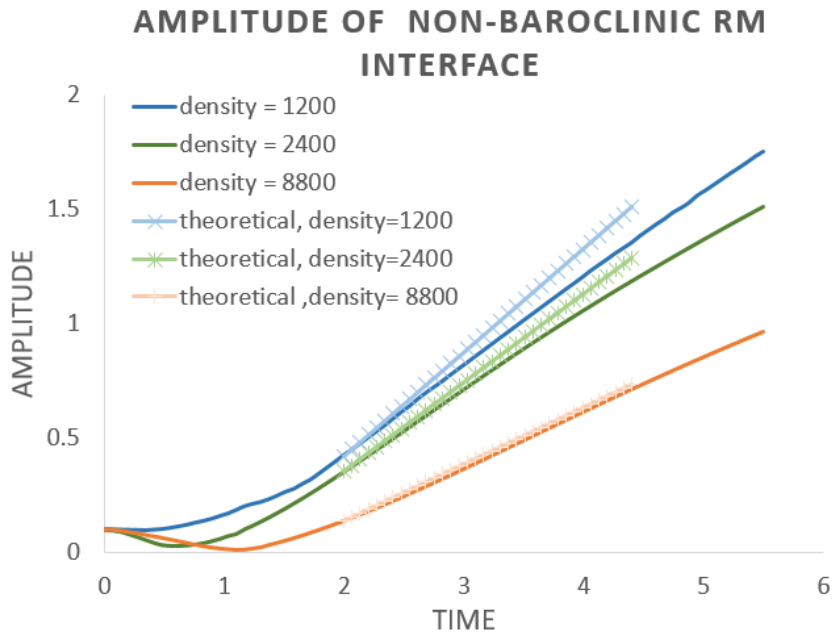

Figure 6.11. Richtmyer-Meshkov Instability growth rate for three different densities of the particles. The three non-marked lines show the amplitude of the particle's cloud in time finding firstly a compression followed by a linear growth. The other marked-lines are the theoretical growths based on Richtmyer-Meshkov growth rate equation 3.30.

The compression when $\rho_{part} = 1200$ is minimal and the theoretical model agree with the simulations. At higher densities of the particle the compression of the cloud become evident. The first fluid is compressed nearly three-fold by the incident shock, but the decompression wave is large due to the density mismatch. This compression is described well by linear theory, numerical simulations and experiments. The growth rates for the simulations are given by the slope of the density lines in Fig. 6.11; this slopes are $m_1 = 0.3828$, $m_2 = 0.3357$ and $m_3 = 0.2991$ for $\rho_{part} = 1200$,$\rho_{part} = 2400$ and $\rho_{part} = 8800$ respectively. Taking all the growth rates from Tables 6.1, 6.2 and 6.3, the theoretical RM growth rates are $\frac{dw_1}{dt} = 0.4527$, $\frac{dw_2}{dt} = 0.3766$ and $\frac{dw_1}{dt} = 0.2381$, which errors are 15%, 10% and 6% for $\rho_{part} = 1200$,$\rho_{part} = 2400$ and $\rho_{part} = 8800$ respectively. We find that the error is higher when ρ_{part} is lower but Equation 3.30 usually agree with the experiments within a 10% error [32].

BIBLIOGRAPHY

[1] U. ALON, J. HECHT, D. MUKAMEL, AND D. SHVARTS, *Scale invariant mixing rates of hydrodynamically unstable interfaces*, Physical review letters, 72 (1994), p. 2867.

[2] U. ALON, J. HECHT, D. OFER, AND D. SHVARTS, *Power laws and similarity of rayleigh-taylor and richtmyer-meshkov mixing fronts at all density ratios*, Physical review letters, 74 (1995), p. 534.

[3] E. BARNEA AND J. MIZRAHI, *A generalized approach to the fluid dynamics of particulate systems: Part 1. general correlation for fluidization and sedimentation in solid multiparticle systems*, The Chemical Engineering Journal, 5 (1973), pp. 171–189.

[4] R. BORGES, M. CARMONA, B. COSTA, AND W. S. DON, *An improved weighted essentially non-oscillatory scheme for hyperbolic conservation laws*, Journal of Computational Physics, 227 (2008), pp. 3191–3211.

[5] L. CLOUTMAN AND M. WEHNER, *Numerical simulation of richtmyer–meshkov instabilities*, Physics of Fluids A: Fluid Dynamics (1989-1993), 4 (1992), pp. 1821–1830.

[6] B. COSTA, W. S. DON, D. GOTTLIEB, AND R. SENDERSKY, *Two-dimensional multi-domain hybrid spectral-weno methods for conservation laws*, technical report, DTIC Document, 2006.

[7] S. DAVIS, T. DITTMANN, G. JACOBS, AND W. DON, *Dispersion of a cloud of particles by a moving shock: Effects of the shape, angle of rotation, and aspect ratio*, Journal of Applied Mechanics and Technical Physics, 54 (2013), pp. 900–912.

[8] S. DAVIS, G. JACOBS, AND W. DON, *Carbuncles in high resolution eulerian-lagrangian simulation of shock-particle-laden flow*, (2013).

[9] G. DIMONTE, *Nonlinear evolution of the rayleigh–taylor and richtmyer–meshkov instabilities*, Physics of Plasmas (1994-present), 6 (1999), pp. 2009–2015.

[10] Z. GAO, W. S. DON, AND Z. LI, *High order weighted essentially non-oscillation schemes for two-dimensional detonation wave simulations*, Journal of Scientific Computing, 53 (2012), pp. 80–101.

[11] J. GIIMM, J. W. GROVE, AND Y. ZHANG, *Three dimensional axisymmetric simulations of fluid instabilities in curved geometry*, WIT Transactions on Engineering Sciences, 29 (1970).

[12] J. GLIMM, J. GROVE, AND Y. ZHANG, *Numerical calculation of rayleigh-taylor and richtmyer-meshkov instabilities for three dimensional axi-symmetric flows in cylindrical and spherical geometries*, Preprint, SUNY at Stony Brook, (1999).

[13] A. HARTEN, B. ENGQUIST, S. OSHER, AND S. R. CHAKRAVARTHY, *Uniformly high order accurate essentially non-oscillatory schemes, iii*, in Upwind and High-Resolution

Schemes, Springer, 1987, pp. 218–290.

[14] M. HERANT AND S. WOOSLEY, *Postexplosion hydrodynamics of supernovae in red supergiants*, The Astrophysical Journal, 425 (1994), pp. 814–828.

[15] R. L. HOLMES, G. DIMONTE, B. FRYXELL, M. L. GITTINGS, J. W. GROVE, M. SCHNEIDER, D. H. SHARP, A. L. VELIKOVICH, R. P. WEAVER, AND Q. ZHANG, *Richtmyer–meshkov instability growth: experiment, simulation and theory*, Journal of Fluid Mechanics, 389 (1999), pp. 55–79.

[16] G. B. JACOBS AND W.-S. DON, *A high-order weno-z finite difference based particle-source-in-cell method for computation of particle-laden flows with shocks*, Journal of Computational Physics, 228 (2009), pp. 1365–1379.

[17] G.-S. JIANG AND C.-W. SHU, *Efficient implementation of weighted eno schemes.*, technical report, DTIC Document, 1995.

[18] D. A. KNOPF, L. M. ANTHONY, AND A. K. BERTRAM, *Reactive uptake of o3 by multicomponent and multiphase mixtures containing oleic acid*, The Journal of Physical Chemistry A, 109 (2005), pp. 5579–5589.

[19] R. J. LEVEQUE, *Finite volume methods for hyperbolic problems*, vol. 31, Cambridge university press, 2002.

[20] X.-D. LIU, S. OSHER, AND T. CHAN, *Weighted essentially non-oscillatory schemes*, Journal of computational physics, 115 (1994), pp. 200–212.

[21] E. LOTH, *Numerical approaches for motion of dispersed particles, droplets and bubbles*, Progress in Energy and Combustion Science, 26 (2000), pp. 161–223.

[22] G. MARKSTEIN, *Flow disturbances induced near a slightly wavy contact surface, or flame front, traversed by a shock wave*, 1957.

[23] W. MARSHALL AND W. RANZ, *Evaporation from drops*, Part I Chem. Engng Prog, 48 (1952), pp. 141–146.

[24] F. MASHAYEK AND R. PANDYA, *Analytical description of particle/droplet-laden turbulent flows*, Progress in energy and combustion science, 29 (2003), pp. 329–378.

[25] M. R. MAXEY AND J. J. RILEY, *Equation of motion for a small rigid sphere in a nonuniform flow*, Physics of Fluids (1958-1988), 26 (1983), pp. 883–889.

[26] R. MEI, R. J. ADRIAN, AND T. J. HANRATTY, *Particle dispersion in isotropic turbulence under stokes drag and basset force with gravitational settling*, Journal of Fluid Mechanics, 225 (1991), pp. 481–495.

[27] E. MESHKOV, *Instability of the interface of two gases accelerated by a shock wave*, Fluid Dynamics, 4 (1969), pp. 101–104.

[28] E. MESHKOV, *Instability of shock-accelerated interface between two media*, Advances in Compressible Turbulent Mixing, 8810234 (1992), p. 473.

[29] F. ODAR AND W. S. HAMILTON, *Forces on a sphere accelerating in a viscous fluid*, Journal of Fluid Mechanics, 18 (1964), pp. 302–314.

[30] L. RAYLEIGH, *Analytic solutions of the rayleigh equation for linear density profiles*, Proc. London. Math. Soc, 14 (1883), pp. 170–177.

[31] L. RAYLEIGH, *Investigation of the character of the equilibrium of an incompressible heavy*, (1900).

[32] R. D. RICHTMYER, *Taylor instability in shock acceleration of compressible fluids*, Communications on Pure and Applied Mathematics, 13 (1960), pp. 297–319.

[33] H. F. ROBEY, J. KANE, B. REMINGTON, R. DRAKE, O. HURRICANE, H. LOUIS, R. WALLACE, J. KNAUER, P. KEITER, D. ARNETT, ET AL., *An experimental testbed for the study of hydrodynamic issues in supernovae*, Physics of Plasmas (1994-present), 8 (2001), pp. 2446–2453.

[34] P. SAFFMAN, *The lift on a small sphere in a slow shear flow*, Journal of fluid mechanics, 22 (1965), pp. 385–400.

[35] H. SCHLICHTING, *Boundary layer theory. mcgraw-hill: New york*, 1979.

[36] B. SHOTORBAN, *Preliminary assessment of two-fluid model for direct numerical simulation of particle-laden flows*, AIAA journal, 49 (2011), pp. 438–443.

[37] B. SHOTORBAN, G. B. JACOBS, O. ORTIZ, AND Q. TRUONG, *An eulerian model for particles nonisothermally carried by a compressible fluid*, International Journal of Heat and Mass Transfer, 65 (2013), pp. 845–854.

[38] D. SNIDER, *An incompressible three-dimensional multiphase particle-in-cell model for dense particle flows*, Journal of Computational Physics, 170 (2001), pp. 523–549.

[39] J.-P. SUAREZ, G. B. JACOBS, AND W.-S. DON, *A high-order dirac-delta regularization with optimal scaling in the spectral solution of one-dimensional singular hyperbolic conservation laws*, SIAM Journal on Scientific Computing, 36 (2014), pp. A1831–A1849.

[40] G. TAYLOR, *The instability of liquid surfaces when accelerated in a direction perpendicular to their planes. i*, in Proceedings of the Royal Society of London A: Mathematical, Physical and Engineering Sciences, vol. 201, The Royal Society, 1950, pp. 192–196.

[41] A. VELIKOVICH, J. DAHLBURG, A. SCHMITT, J. GARDNER, L. PHILLIPS, F. COCHRAN, Y. CHONG, G. DIMONTE, AND N. METZLER, *Richtmyer–meshkov-like instabilities and early-time perturbation growth in laser targets and z-pinch loads*, Physics of Plasmas (1994-present), 7 (2000), pp. 1662–1671.

[42] C. WANG AND P. CHENG, *A multiphase mixture model for multiphase, multicomponent transport in capillary porous mediai. model development*, International journal of heat and mass transfer, 39 (1996), pp. 3607–3618.

[43] Z. WANG, C. WANG, AND K. CHEN, *Two-phase flow and transport in the air cathode of proton exchange membrane fuel cells*, Journal of Power Sources, 94 (2001), pp. 40–50.

[44] F. M. WHITE AND I. CORFIELD, *Viscous fluid flow*, vol. 3, McGraw-Hill New York,

2006.

[45] N. J. ZABUSKY, *Vortex paradigm for accelerated inhomogeneous flows: Visiometrics for the rayleigh-taylor and richtmyer-meshkov environments*, Annual Review of Fluid Mechanics, 31 (1999), pp. 495–536.

[46] J. ZHU AND J. QIU, *A new fifth order finite difference weno scheme for solving hyperbolic conservation laws*, Journal of Computational Physics, 318 (2016), pp. 110–121.

APPENDIX A

VARIABLES USED IN THE SIMULATION CREATED WITH FORTRAN

VARIABLES USED IN THE SIMULATION CREATED WITH FORTRAN

In this appendix we explain some of the most important variables used in this work. The code has been created with FORTRAN and we have used MATLAB for the plots.

A.1 NUMBER DENSITY Φ

We use the variable Φ to assign the contribution of each particle to the cell points where the particle is located in terms of quantity of particles. What is more, with this parameter we easily can see where are more particles and which are the cells with more particles in it.

If we have a particle in a rectangular cell as shown in Fig. A.1 we split the cell in four areas. The distribution of the area into each cell point is related with the proximity of each particle into the four points of the cell. For example, The cell point marked with a red circle in Fig. A.1 will be assigned with the area $distx2 \times disty2$ because in this case, the particle is closer to the grid point $matrix\_phi(npart\_locx\_phi, npart\_locy\_phi)$ so the area assigned to this point is bigger than the area assigned to the other three grid points.

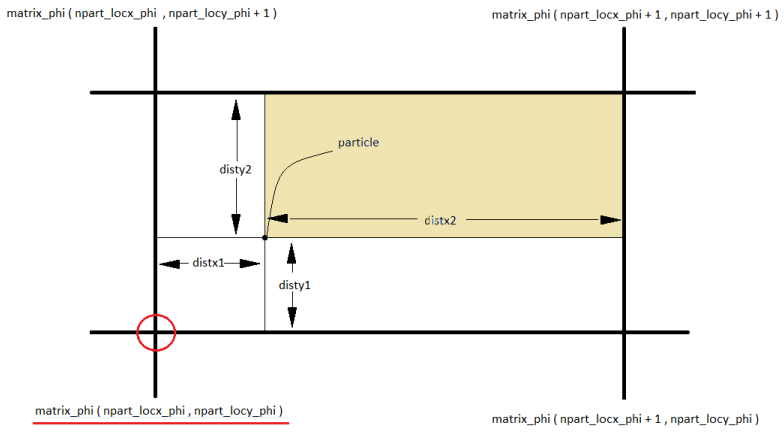

Figure A.1. Different variables used to calculate some of the particle parameter such as Φ or $\tilde{u}$.

Following the code, firstly we initialize the matrix to zero and we start the loop from the particle number 1 to the last particle (we have $Npart$ number of particles). Secondly we calculate the exact location of each particle in x and y direction ($npart\_loc\_x$ and $npart\_loc\_y$

respectively) and the distances from the particle to each grid point (4 points in total per particle).Finally, for each particle, we assign the areas to the grid points.

A.2 AVERAGE OF THE PARTICLE'S VELOCITY IN x DIRECTION $\tilde{u}$

The calculus of $\tilde{u}$ is similar to Φ. In this case we distribute the U velocity of each particle using the same areas shown in Appendix A.1. Once you have run the code we have a parameter like so $\tilde{u\phi}$. Making use of the next equation for each particle we can have the final value of $\tilde{u}$.

$$\tilde{u} = \frac{\tilde{u\phi}}{\tilde{\phi}} = \tilde{u} \tag{A.1}$$

As we can see in Fig.A.2 we have in red color the grid points where the particles are going fast and in blue color where there are few particles or they are going slow. In white color we have no particles.

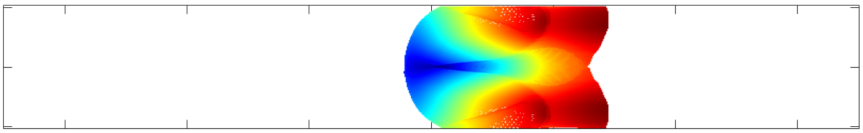

Figure A.2. Example of $\tilde{u}$ parameter where we can find in red color how the particles are faster than in blue color.

APPENDIX B

ADDITIONAL RESULTS

ADDITIONAL RESULTS

We decided to add every single parameter of the simulation in each figure so we can see at first sight and in one page the complete development of the parameter. The fist step starts at $time = 0$ and goes until $time = 5.5$. The resolution of the figures are 1.1 so we will have six plots per parameter.

The first figure in page 50 shows the progress of the particle cloud in time in a density profile (Fig. B.1). The next figure in page 51 we show how Φ changes with time (Fig.B.2). The third figure shows te absolute value of the vorticity explained as

$$|\frac{\partial v}{\partial x} - \frac{\partial u}{\partial y}| \tag{B.1}$$

With this variable we easily can see the local spinning motion of a continuum near some point (the tendency of something to rotate). The forth figure in page 53 shows the variable $\tilde{u}$ explained in appendix A.2 (Fig. B.4). Fig. B.5 shows schilieren plot of the simulations, which is a method for detecting regions of different densities. This method is based on the next equation

$$\sqrt{(\frac{\partial \rho}{\partial x})^2 + (\frac{\partial \rho}{\partial y})^2} \tag{B.2}$$

In Fig. B.7, B.8, B.9,B.10, B.11, B.12 and B.13 we show the velocity in y-direction, Temperature, Mach, Vorticity, pressure, total Temperature and Total Pressure of the fluid.

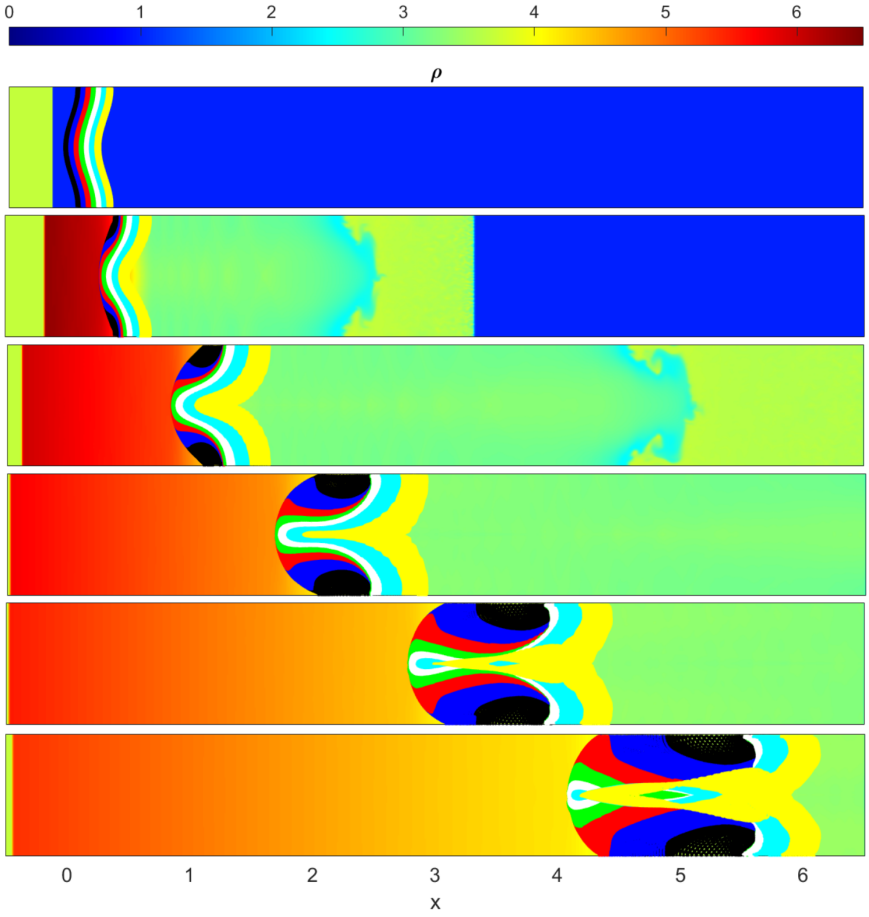

Figure B.1. Progress of the particles which are color coded so we can trace their motion and understand their origin when the flow develops. The background of the simulation is the density of the fluid at times 0, 1.1, 2.2, 3.3, 4.4 and 5.5 respectively.

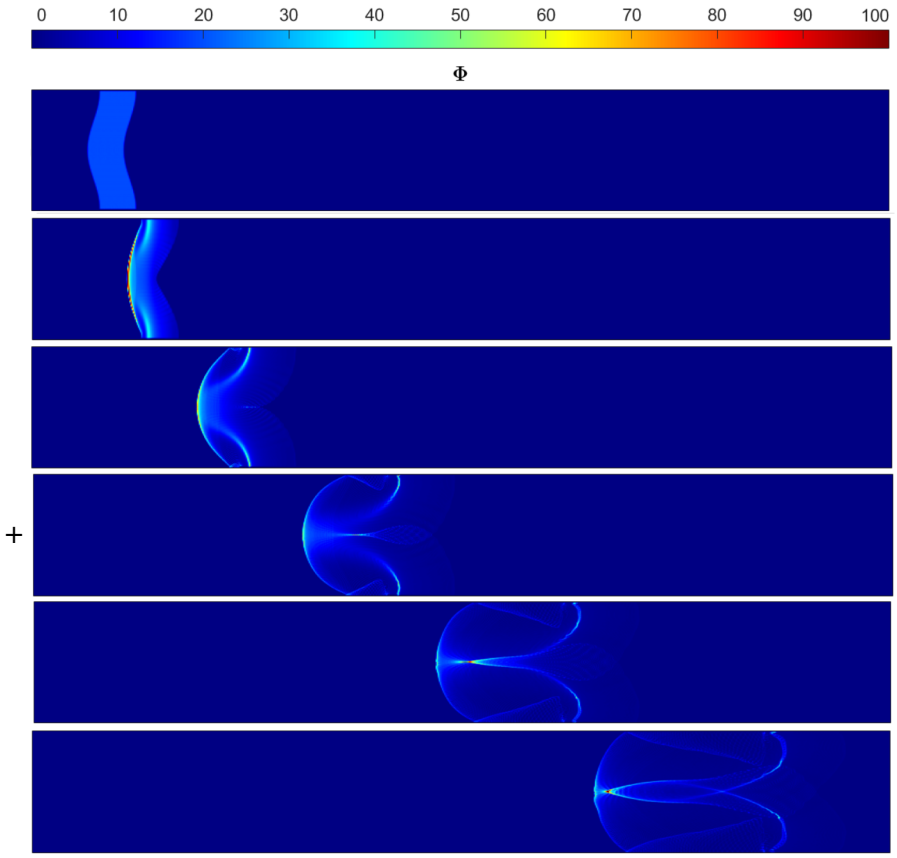

Figure B.2. Variable Φ as a number density of the particles at times 0, 1.1, 2.2, 3.3, 4.4 and 5.5 respectively. What we do with this variable is assigning the contribution of each particle to the cell points where particle is located in terms of quantity of particles.

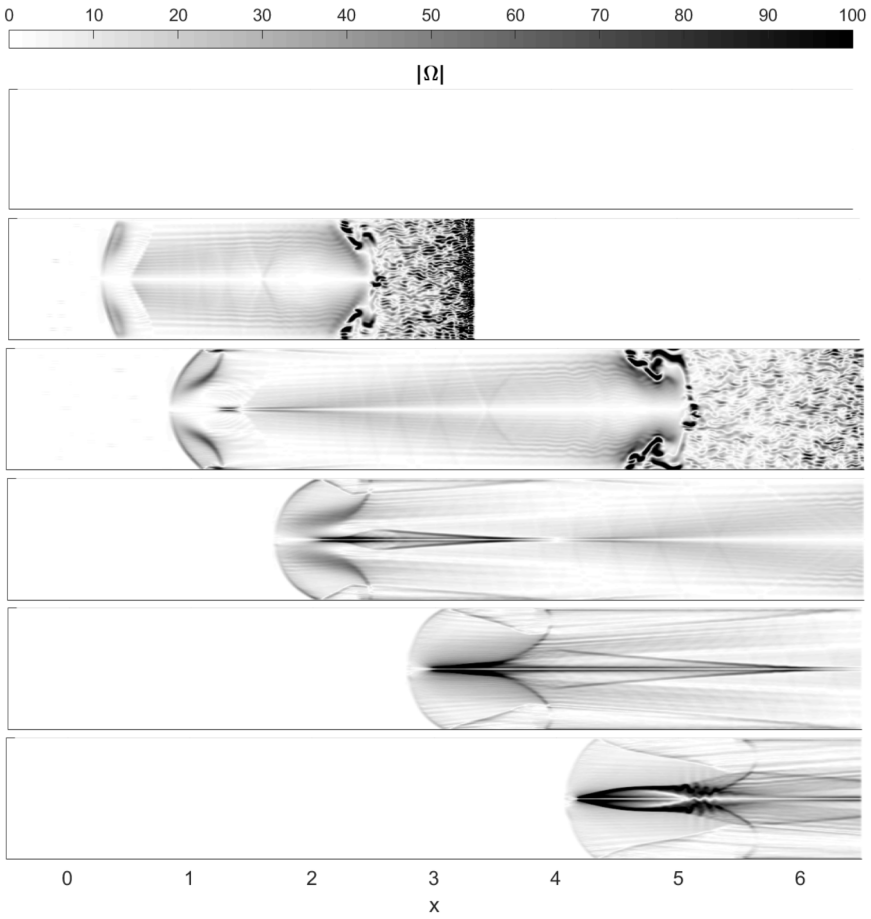

Figure B.3. Absolute valor of the vorticity defined as $|\frac{\partial v}{\partial x} - \frac{\partial u}{\partial y}|$ for time 0, 1.1, 2.2, 3.3, 4.4 and 5.5.

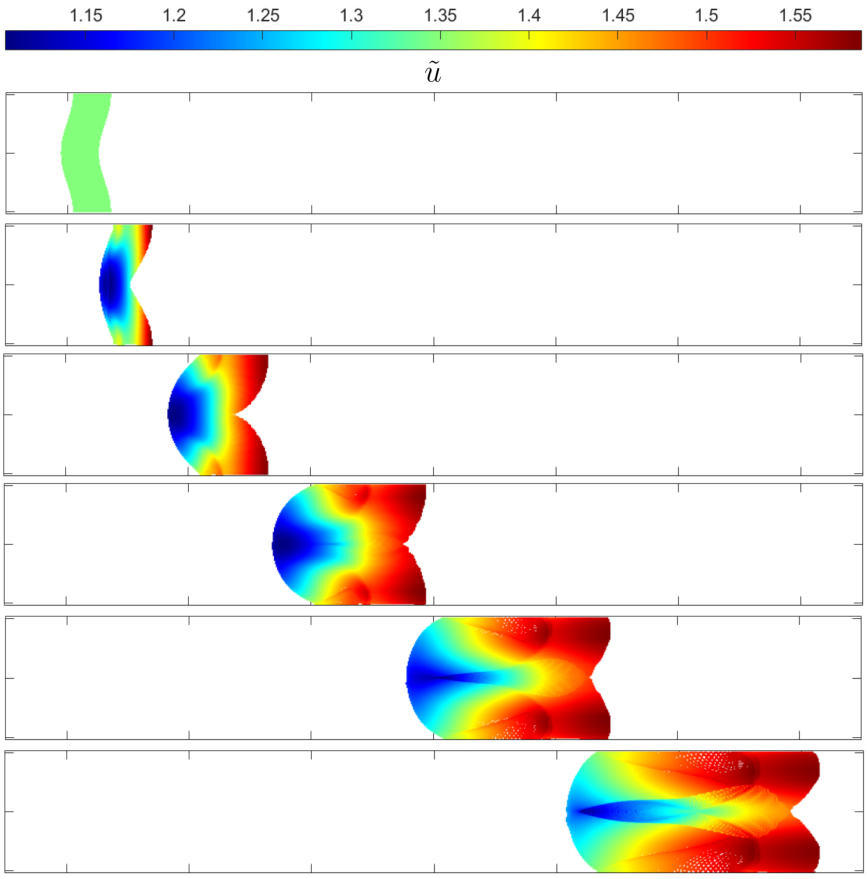

Figure B.4. Velocity of the particles at times 0, 1.1, 2.2, 3.3, 4.4 and 5.5. We easily can see the differences between the velocity of the particle where the particles leading the growth of the cloud,thus, the growth of Richtmyer-Meshkov Instability.

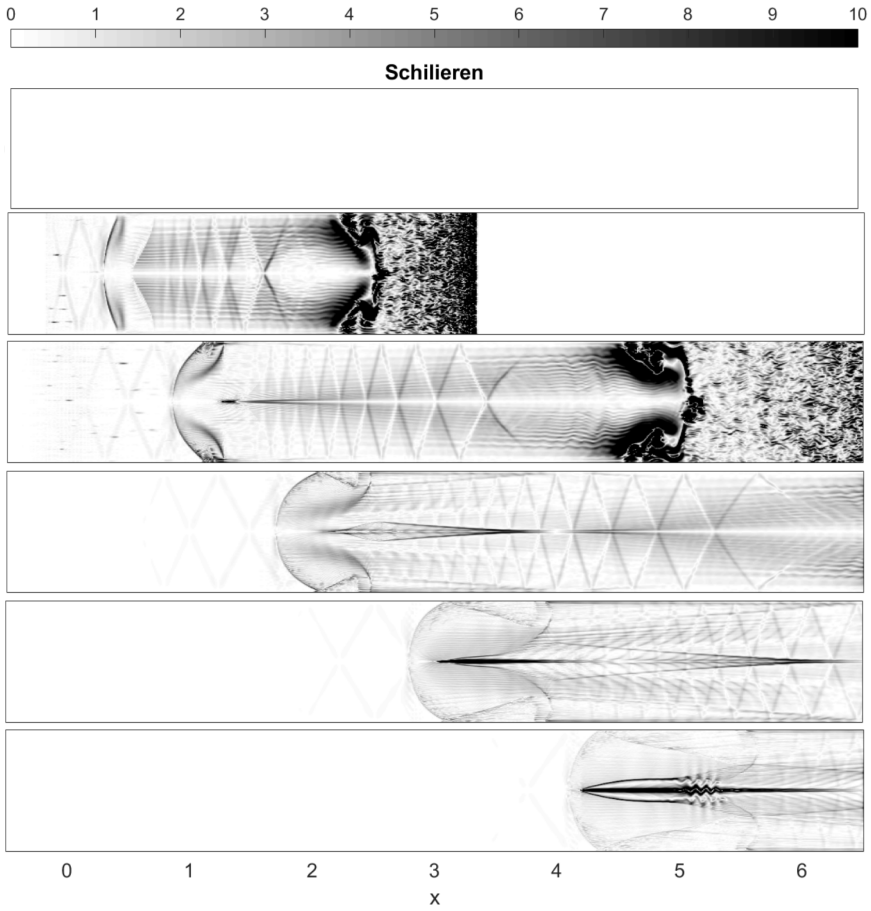

Figure B.5. Schilieren method for visualization of the simulation from time=0.0 to time=5.5. In this figures we easily can see the supersonic instabilities in shape of lines produced by the transmitted shock.

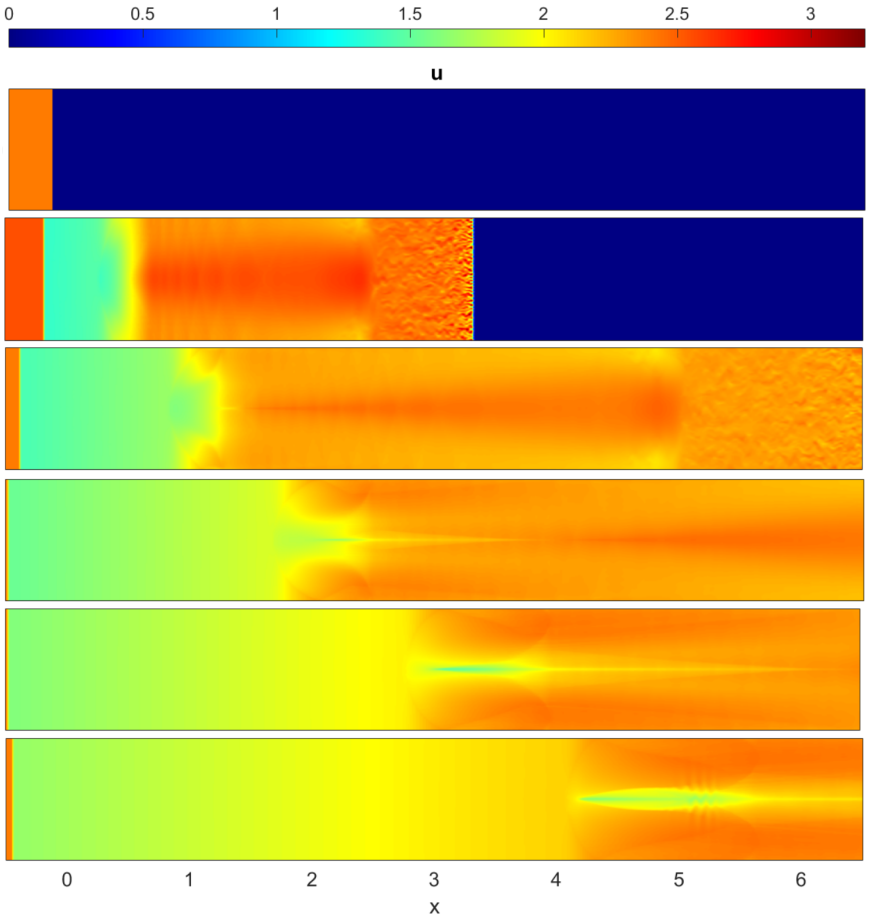

Figure B.6. Velocity of the fluid in x direction at times 0, 1.1, 2.2, 3.3, 4.4 and 5.5 respectively.

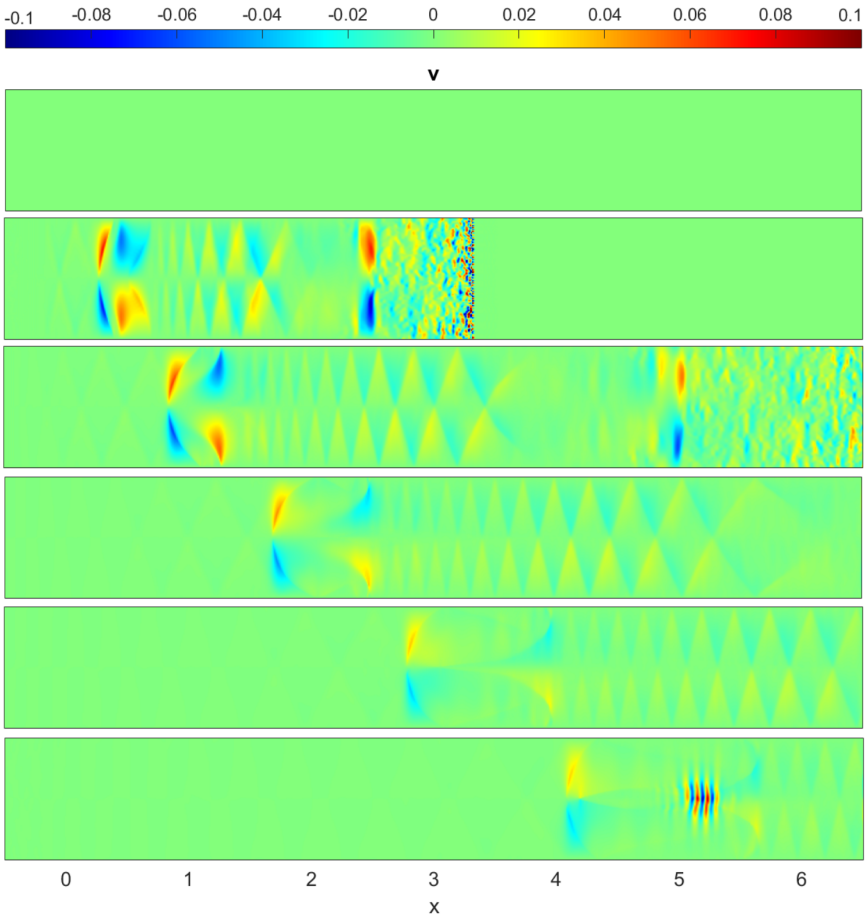

Figure B.7. Velocity of the fluid in y direction at times 0, 1.1, 2.2, 3.3, 4.4 and 5.5 respectively.

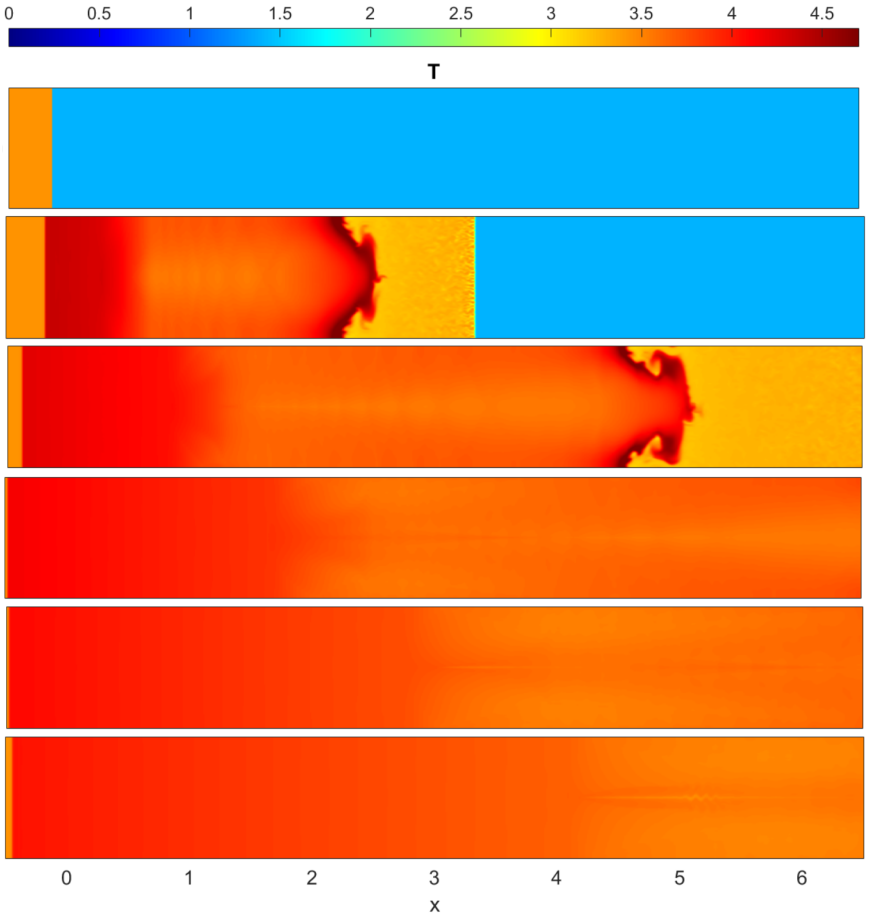

Figure B.8. Temperature of the fluid at times 0, 1.1, 2.2, 3.3, 4.4 and 5.5 respectively. We can see that after the particle's cloud, the Temperature is lower due to the heat transfer from the fluid to the particles.

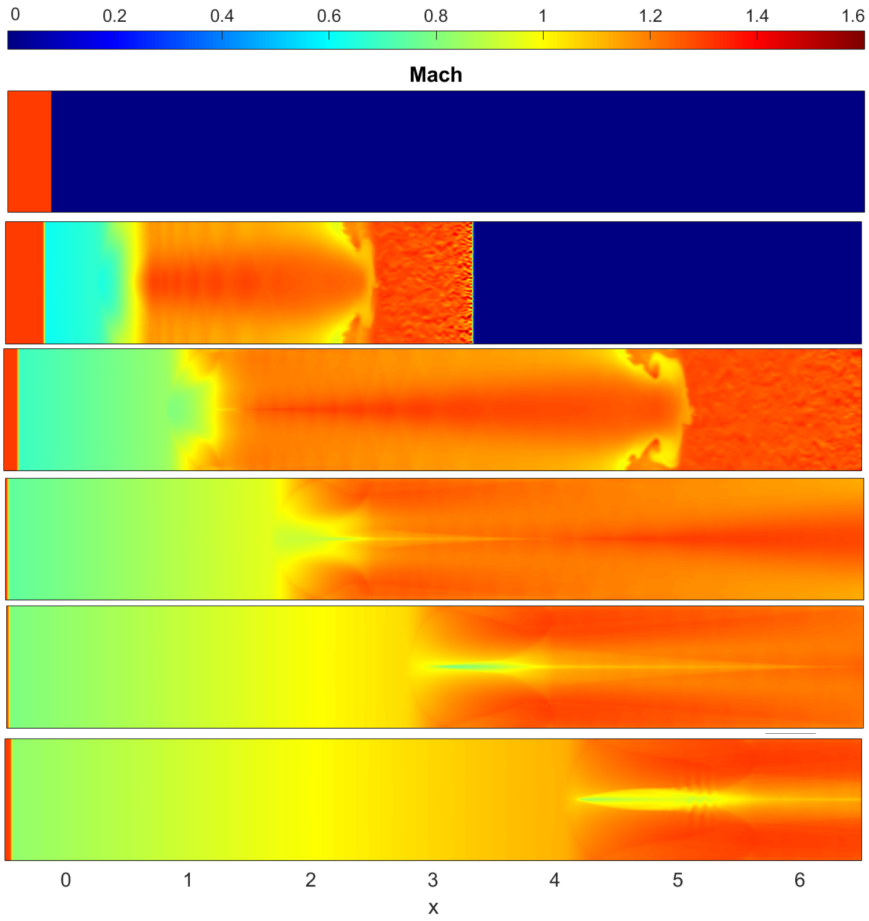

Figure B.9. Mach Number of the fluid at times 0, 1.1, 2.2, 3.3, 4.4 and 5.5 respectively. Before the cloud we find a reflected shock moving back to x=-0.5. This is due to the subsonic flow.

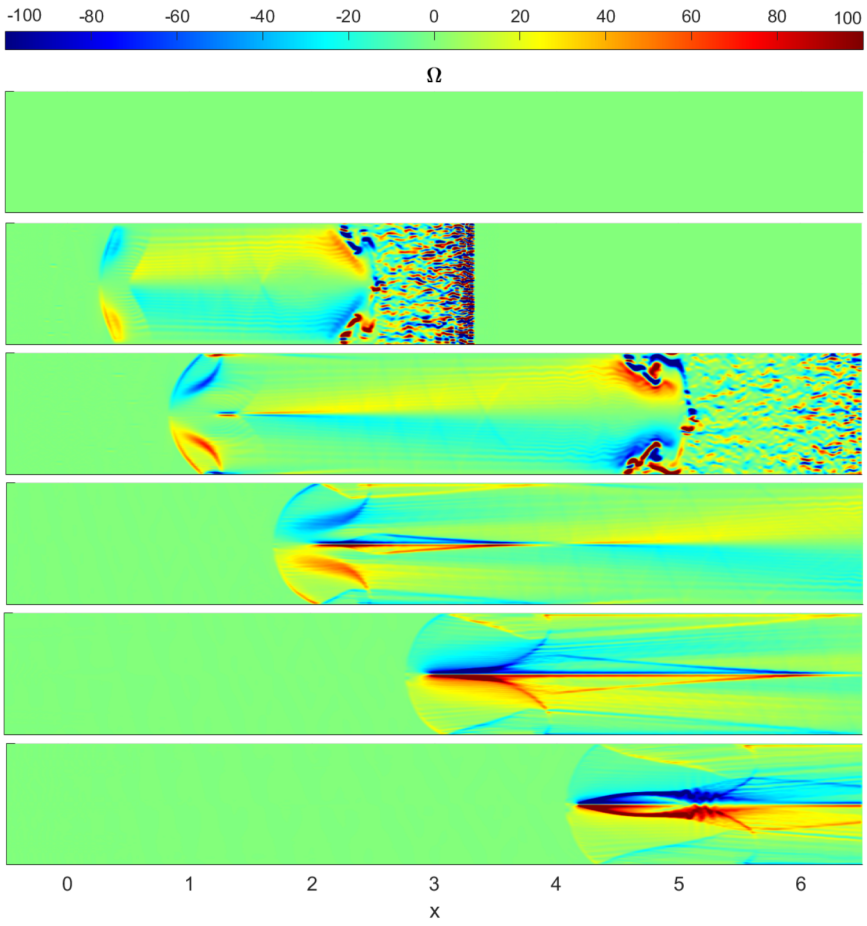

Figure B.10. Vorticity of the fluid at times 0, 1.1, 2.2, 3.3, 4.4 and 5.5 respectively. The bar of the simulation is limited at the value of 100 so we can see better the vorticity in the non-baroclinic interface.

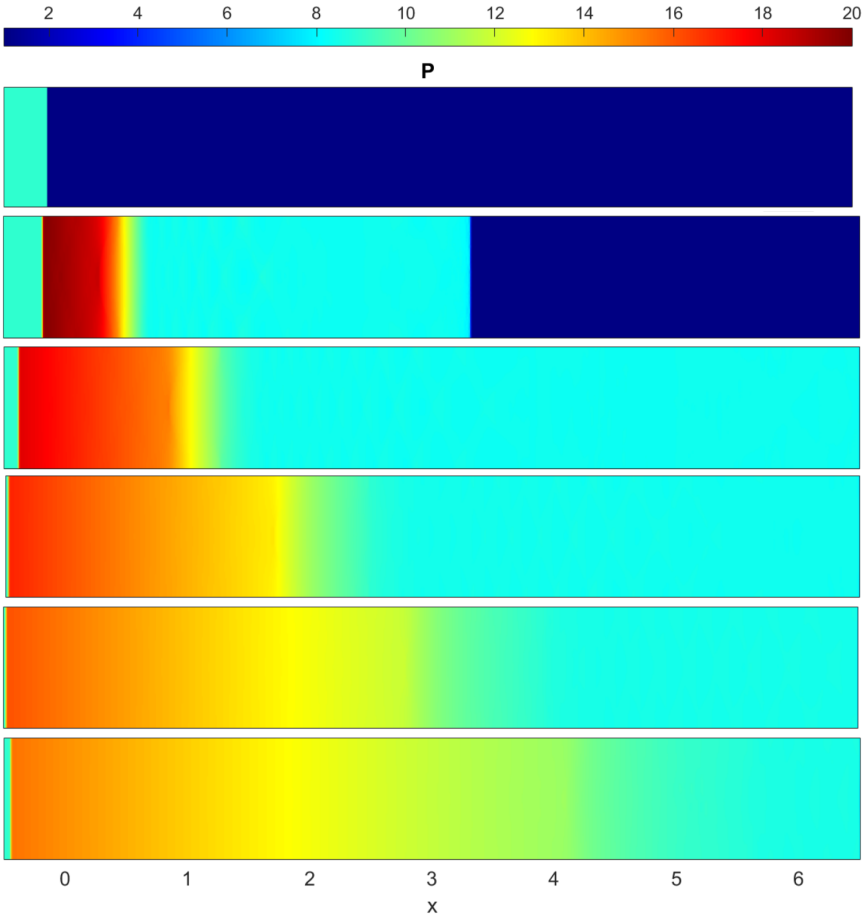

Figure B.11. Pressure of the fluid at times 0, 1.1, 2.2, 3.3, 4.4 and 5.5 respectively.

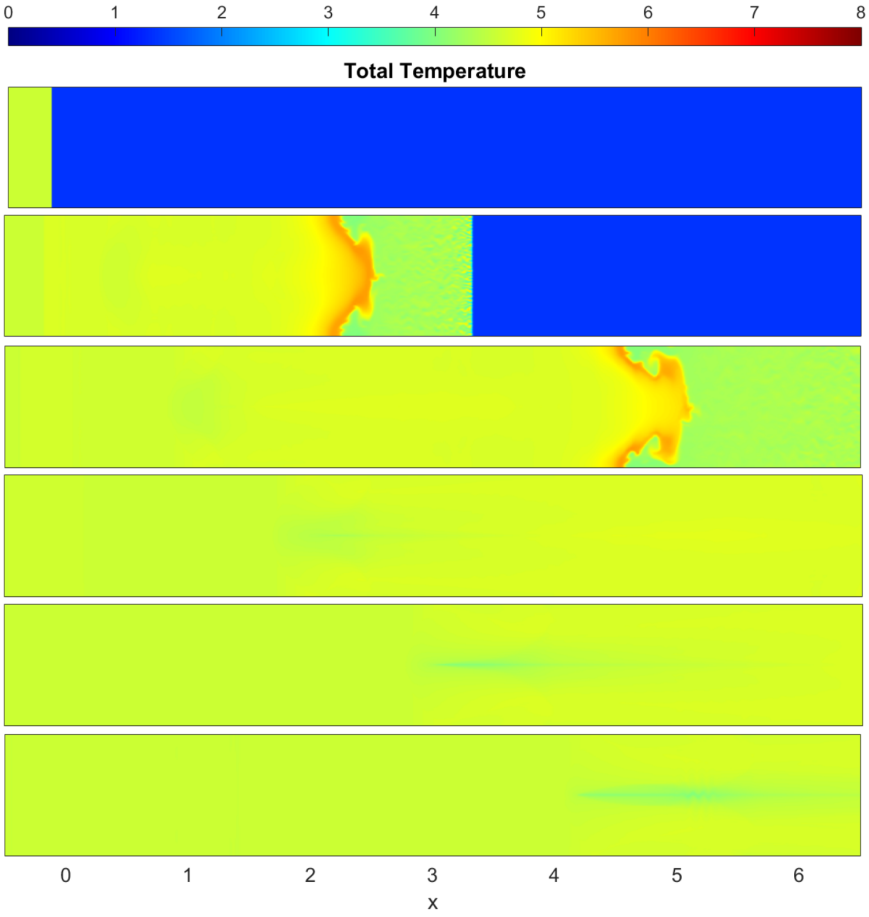

Figure B.12. Total Temperature of the fluid at times 0, 1.1, 2.2, 3.3, 4.4 and 5.5 respectively. In the non-baroclinic interface the total pressure remains constant due to absent of heat transfer.

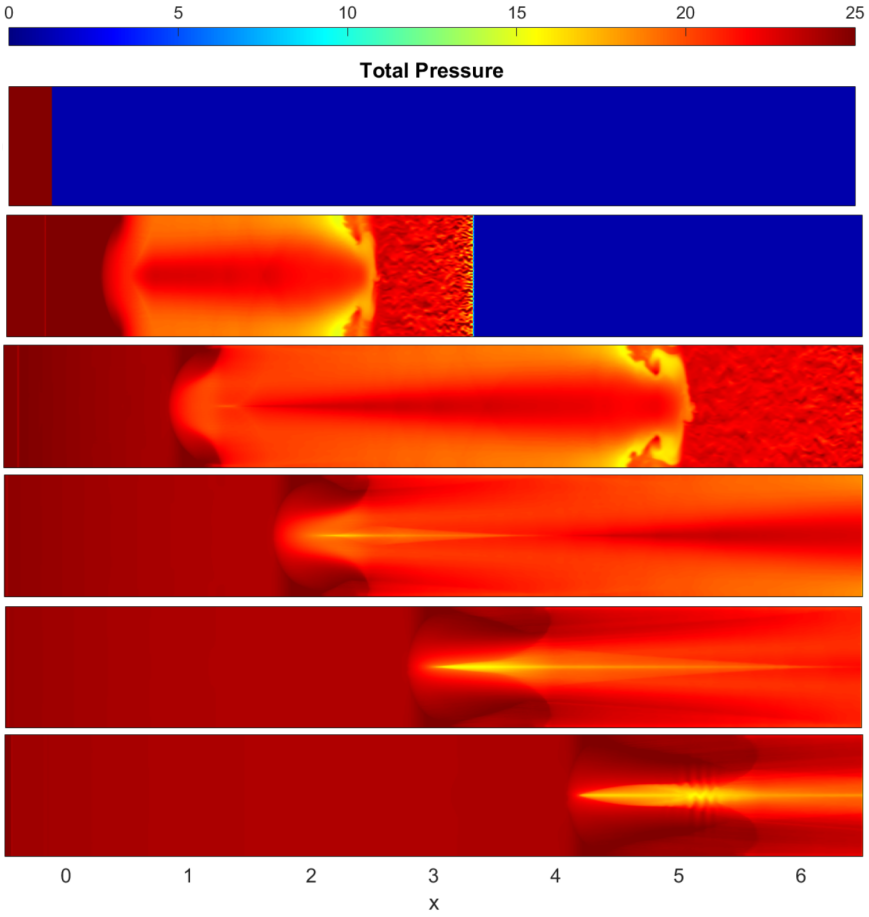

Figure B.13. Total Pressure of the fluid at times 0, 1.1, 2.2, 3.3, 4.4 and 5.5 respectively.